A Domain Decomposition Technique for Small Amplitude Wave Interactions with Shock Waves

U S Vevek, B. Elhadidi and W.L. Chan*

School of Mechanical and Aerospace Engineering, Nanyang Technological University

50 Nanyang Avenue, Singapore 639798

Abstract

In this paper, a domain decomposition technique in the finite volume framework is presented to propagate small amplitude acoustic and entropy waves in a linearized Euler region and simulate the interaction of these waves with an initially steady normal shock in a nonlinear region. An overset method is used to two-way couple the linear and nonlinear regions that overlap each other. Linearized solvers alone cannot capture this interaction due to the discontinuity encountered at shocks. On the other hand, nonlinear solvers based on second order shock-capturing schemes will result in excessive dissipation and dispersion for the small disturbances. The domain decomposition technique provides a good balance between minimizing dissipation & dispersion errors while enabling nonlinear shock-acoustic interactions. To preserve low dispersion and dissipation, a DRP scheme is used to simulate the incoming and outgoing waves in the linear region. To capture the shock wave interaction and motion, a hybrid central-upwind flux scheme is used in the nonlinear region that contains the shock. Grid sensitivity studies for an acoustic wave propagating in stationary flow were performed to compare the linear, nonlinear, and domain decomposition solvers. The nonlinear solver required ten times the mesh resolution to achieve similar accuracy as the linear solver, resulting in a forty-fold increase in computational time. For modest cell size ratios, the domain decomposition solver reduced the computational time by a factor of three compared to the nonlinear solver while achieving similar accuracy. Interaction of standing shocks with acoustic and entropy waves of amplitudes $\epsilon = \pm 10^{-2}$ and $\pm 10^{-5}$ was investigated using the domain decomposition technique. The numerical results for $\epsilon = \pm 10^{-2}$ compared well with the linearized interaction analysis (LIA) with less than 3% discrepancy in terms of the amplification factors. The domain decomposition technique acts as a low pass filter that averages the post-shock oscillations generated by the slow-moving shocks in the nonlinear region, resulting in the correct amplification factors in the linear region. For the smaller amplitudes of $\epsilon = \pm 10^{-5}$, the amplification factors deviated from LIA predictions by up to 70%.

*Corresponding author: chan.wl@ntu.edu.sg

Numerical results suggest that the large discrepancy for the small amplitude cases is due to insufficient mesh resolution for capturing extremely slow-moving shocks.

1 Introduction

Modelling the interaction of acoustic, vortical, and entropy waves with shock waves is essential for the understanding of jet noise and mitigation efforts in supersonic exhausts [1]. Exhaust nozzles can operate in imperfectly expanded regimes, resulting in several shock waves. Acoustic disturbances generated inside the engine from combustion and turbine/stator interaction amplify as they interact with shock waves. The increase in amplitude has several consequences, such as increased structural fatigue loading and amplified tonal noise. As the acoustic waves interact with the shock waves, they not only amplify, but generate additional vortical and entropy waves that can further interact with the turbulence in the flow to increase the broadband noise levels [2].

Traditionally, in computational aeroacoustics, sound propagation is modelled by assuming small perturbations about a mean state. Small perturbations could be represented as a superposition of acoustic, vorticity, and entropy waves using Kovasznay's decomposition [3]. As viscous effects are minimal for small disturbances, linearized Euler equations (LEE) can be applied with accuracy. To minimize the numerical dispersion and diffusion errors, especially for problems involving wave propagation over long distances [4], the LEE are solved using a dispersion-relation-preserving (DRP) scheme [5], which is best implemented on uniform Cartesian grids. The LEE are applicable for mean flows that are smooth and continuous but will lead to erroneous predictions for flows with large gradients and discontinuities [6]. Furthermore, linearized interaction analyses (LIA) performed by Ribner [7, 8] and Moore [9] have revealed that the interaction of small disturbances with shocks waves (i) modifies the amplitudes of the incoming waves, (ii) generates additional waves, and (iii) causes the shock wave to move. This nonlinear phenomenon, which cannot be accounted for by the linear solver, requires a nonlinear simulation that is either excessively diffusive and/or dispersive or prohibitively expensive for propagation of small waves over long distances. To circumvent the shortcomings of the linear and nonlinear solvers in simulating the interaction of small disturbance waves with shock waves, the current work uses the concept of domain decomposition to couple the LEE and Euler equations [10]. Though direct numerical simulations (DNS) have been performed in the past to study the interaction of a shock wave with turbulence [11-16] and acoustic waves [17], the current work appears to be the first to use domain decomposition to study the interaction of a shock wave with small perturbations.

Domain decomposition has become the method of choice for solving coupled problems in recent times since it provides the flexibility to solve each set of governing equations using the most suitable numerical methods on the most optimal grids. One of the popular domain decomposition methods for coupled flow/acoustic problems involves solving the compressible Navier-Stokes equations and the nonlinear Euler equations on separate, non-overlapping grids using finite volume (FV) and discontinuous Galerkin methodologies, respectively [18-22]. The domain decomposition technique proposed in this paper possesses several innovative ideas compared to past studies. In the proposed technique, the computational domain is divided into linear and nonlinear regions in which the linearized and nonlinear Euler equations are solved, respectively. Both sets of governing equations are formulated in the FV framework, but they are solved using different spatial discretization schemes on different grids. The Euler equations are solved using a second order hybrid central-upwind scheme that allows the use of non-uniform grids. This provides the flexibility to achieve a fine mesh resolution when capturing the shock motion while limiting the extent of this finely resolved region to a small area in the vicinity of the shock. As a result, the dispersion errors incurred by the second order schemes can be minimized. The LEE are solved in terms of the perturbed conserved variables using a DRP scheme on uniform Cartesian grids. The formulation of the linearized fluxes accounts for spatially varying mean states in a straightforward manner. The linear region can be used to extend the computational domain to account for wave propagation over large distances. This approach is more efficient than using a purely nonlinear solver which demands fine grids to negate the poor resolving properties of second order schemes. The linear and nonlinear regions are two-way coupled using overset methods that involve a combination of volumetric mapping and interpolation. Last but not least, non-reflecting boundary conditions have been implemented in the form of sponge layers [23] along the boundaries of the linear region. Artificial viscous damping is applied in the sponge layers to prevent the re-entry of reflected waves into the domain. Compared to more sophisticated methods (e.g. perfectly matched layers [24], characteristic boundary conditions [25], and radiation/outflow conditions [26]), sponge layers are simple to implement and more flexible in handling complex geometries. Mani [27] has shown that, with proper tuning, sponge layers can deliver comparable performance to the more sophisticated methods.

The objectives of this paper are two-fold. The first objective is to present the domain decomposition technique and assess its properties. Though the technique has been developed in a general multi-dimensional form, the discussion in this paper is restricted to a one-dimensional case for the sake of simplicity of analysis. The second objective is to apply the technique to compute the interaction of small amplitude acoustic and entropy waves with standing shock waves. The paper is organized as follows. First, the solution methodologies for the nonlinear and linear regions are presented in Section 2, detailing the two-way coupling between the regions and implementation of the sponge layers. Next, the performance of the linear solver is validated and the results of the proposed domain decomposition for benchmark cases are presented in Section 3. In addition, results for the interaction of acoustic/entropy waves with a normal shock are discussed in detail. Then, the concluding remarks are summarized in Section 4. Lastly, a simplified one-dimensional linear analysis of shock-wave interaction is provided in the Appendix.

2 Method

2.1 Finite Volume Approach

Inviscid gas dynamics is governed by the Euler equations given in conservative form by,

$$\partial_t \mathbf{Q} + \nabla \cdot \mathrm{F}(\mathbf{Q}) = \mathbf{0}, \tag{1}$$

where $\mathbf{Q} = (\rho,\ \rho\boldsymbol{u},\ \rho e_t)^{\mathrm{T}}$ represents the vector of conserved variables and $\mathrm{F}(\mathbf{Q})$ represents the inviscid flux function. Assuming calorically perfect ideal gas, $\mathrm{F}(\mathbf{Q})$ is given by,

$$\mathrm{F}(\mathbf{Q}) = \begin{pmatrix} \rho\boldsymbol{u} \\ \rho\boldsymbol{u}\boldsymbol{u} + p\mathbf{I} \\ \dfrac{\gamma p\boldsymbol{u}}{\gamma - 1} + \dfrac{1}{2}\rho\|\boldsymbol{u}\|^2\boldsymbol{u} \end{pmatrix}, \tag{2}$$

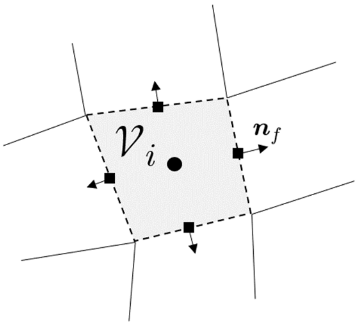

Figure 1: Nomenclature for finite volume approach. The circle, squares and arrows represent the cell centroid, face centroids and face unit normal vectors, respectively.

where $\gamma = 1.4$ is the specific heat ratio and $\mathbf{I}$ is the 3×3 Kronecker delta tensor. In finite volume, the solution is obtained in terms of the cell averages of the conserved variables. Denoting the cell average over cell $\mathcal{V}_i$ as $\mathbf{Q}_i$, its instantaneous rate of change is equal to the net flux across the cell boundary $\partial \mathcal{V}_i$ which is approximated as follows:

$$\frac{d\mathbf{Q}_i}{dt} \approx -\frac{1}{|\mathcal{V}_i|} \sum_{f \in \partial \mathcal{V}_i} \hat{\mathrm{F}}_n S_f \tag{3}$$

$\hat{\mathrm{F}}_n$ is the numerical approximation to the face-normal flux. The subscript n represents the normal $\boldsymbol{n}_f$ as illustrated in Figure 1. $|\mathcal{V}_i|$ denotes the cell volume and S_f denotes the face area. To minimize numerical dissipation without sacrificing stability, the numerical flux $\hat{\mathrm{F}}_n$ was taken to be the weighted average of a central flux $\hat{\mathrm{F}}_n^{ctr}$ and an upwind flux $\hat{\mathrm{F}}_n^{upw}$,

$$\hat{\mathrm{F}}_n = (1 - \Theta)\hat{\mathrm{F}}_n^{ctr} + \Theta \hat{\mathrm{F}}_n^{upw}, \tag{4}$$

where Θ is a suitable shock sensor which is zero when the solution is smooth and reaches a maximum value of unity near shocks. In the present study, the Bhagatwala-Lele shock sensor [28] with the modification proposed by U S Vevek, *et al.* [29] was used. $\hat{\mathrm{F}}_n^{ctr}$ was computed using linear interpolations of the primitive variables $\mathbf{U} = (\rho,\ \boldsymbol{u},\ p)^{\mathrm{T}}$ at the face centroids $\boldsymbol{x}_f$:

$$\hat{\mathrm{F}}_n^{ctr}(\mathbf{U}_f) = \begin{pmatrix} \rho_f u_f \\ \rho_f \boldsymbol{u}_f u_f + p_f \boldsymbol{n}_f \\ \dfrac{\gamma}{\gamma-1} p_f u_f + \dfrac{1}{2}\rho_f \|\boldsymbol{u}_f\|^2 u_f \end{pmatrix}, \qquad u_f \equiv \boldsymbol{u}_f \cdot \boldsymbol{n}_f. \tag{5}$$

For the upwind numerical flux $\hat{\mathrm{F}}_n^{upw}$, the HLLC flux scheme [30] with wave speed computed based on Roe average [31] was used for its simplicity and its ability to capture isolated shock waves exactly. $\hat{\mathrm{F}}_n^{upw}$ was computed based on directional (biased) interpolations of the primitive variables computed using total-variation-diminishing schemes [32, 33] with the van Leer limiter function [34].

2.1.1 Linearized Euler Fluxes

In the far field (away from shock waves and scattering surfaces), the solution $\mathbf{Q}(\boldsymbol{x},t)$ can be modelled as a small perturbation $\mathbf{Q}'(\boldsymbol{x},t)$ linearized about a mean state $\overline{\mathbf{Q}}(\boldsymbol{x},t)$, i.e. $\mathbf{Q}(\boldsymbol{x},t) = \overline{\mathbf{Q}}(\boldsymbol{x},t) + \mathbf{Q}'(\boldsymbol{x},t)$, such that $|\mathbf{Q}'(\boldsymbol{x},t)| \ll |\overline{\mathbf{Q}}(\boldsymbol{x},t)|$. The mean state satisfies the nonlinear governing equation below:

$$\partial_t \overline{\mathbf{Q}} + \nabla \cdot \mathrm{F}(\overline{\mathbf{Q}}) = \mathbf{0} \tag{6}$$

Subtracting Eq. (6) from Eq. (1) results in the governing equation for the small perturbation variables in conservative form,

$$\partial_t \mathbf{Q}' + \nabla \cdot \mathrm{F}'(\overline{\mathbf{Q}}, \mathbf{Q}') = \mathbf{0}, \tag{7}$$

where $\mathrm{F}'(\overline{\mathbf{Q}}, \mathbf{Q}') = \mathrm{F}(\overline{\mathbf{Q}} + \mathbf{Q}') - \mathrm{F}(\overline{\mathbf{Q}})$ is the small perturbation flux. The finite volume procedure can be applied to Eq. (7) to arrive at the following semi-discrete equation for the cell average of the perturbed conserved variables $\mathbf{Q}_i'$,

$$\frac{d\mathbf{Q}_i'}{dt} = -\frac{1}{|\mathcal{V}_i|} \sum_{f \in \partial \mathcal{V}_i} \hat{\mathrm{F}}_n' S_f, \tag{8}$$

where $\hat{\mathrm{F}}_n'$ is the perturbed face-normal flux approximated using only the non-dissipative central fluxes,

$$\hat{\mathrm{F}}_n' = \hat{\mathrm{F}}_n^{ctr}(\overline{\mathbf{U}}_f + \mathbf{U}_f') - \hat{\mathrm{F}}_n^{ctr}(\overline{\mathbf{U}}_f). \tag{9}$$

Unlike $\hat{\mathrm{F}}_n^{ctr}$ in Eq. (4) which is computed using a second order linear scheme, $\hat{\mathrm{F}}'_n$ is computed using a fourth order group-velocity-optimized DRP scheme [35]. On a uniform Cartesian mesh, this six-cell interpolation scheme can be implemented as,

$$\phi_{i+1/2} = \alpha_1(\phi_i + \phi_{i+1}) + \alpha_2(\phi_{i-1} + \phi_{i+2}) + \alpha_3(\phi_{i-2} + \phi_{i+3}), \tag{10}$$

where the coefficients $\alpha_1 = 0.625019618873956850$, $\alpha_2 = -0.145862761644268701$ and $\alpha_3 = 0.02084314277031176$. More details on the finite volume formulation of the DRP scheme can be found in the work of Popescu, *et al.* [36].

Expanding Eq. (9) and ignoring the second and higher order product terms results in,

$$\hat{\mathrm{F}}'_n = \begin{pmatrix} \varphi \\ \varphi\overline{\boldsymbol{u}}_f + \bar{\rho}_f \boldsymbol{u}'_f \bar{u}_f + p'_f \boldsymbol{n}_f \\ \dfrac{\gamma}{\gamma - 1}\left[p'_f \bar{u}_f + \bar{p}_f u'_f\right] + \dfrac{1}{2}\varphi\|\overline{\boldsymbol{u}}_f\|^2 + \bar{\rho}_f(\overline{\boldsymbol{u}}_f \cdot \boldsymbol{u}'_f)\bar{u}_f \end{pmatrix}, \tag{11}$$

where $\varphi = \rho'_f \bar{u}_f + \bar{\rho}_f u'_f$ is the linearized mass flux. The perturbed velocity $\boldsymbol{u}'$ and pressure p' can be computed from the following relationships prior to interpolation:

$$\boldsymbol{u}' = \frac{\overline{(\rho\boldsymbol{u})} + (\rho\boldsymbol{u})'}{\bar{\rho} + \rho'} - \overline{\boldsymbol{u}} \tag{12}$$

$$p' = (\gamma - 1)\left[\overline{(\rho e_t)} + (\rho e_t)' - \frac{1}{2}(\bar{\rho} + \rho')\|\boldsymbol{u} + \boldsymbol{u}'\|^2\right] - \bar{p} \tag{13}$$

The semi-discrete equations Eq. (3) and Eq. (8) were time marched in tandem using a fourth order low-dissipation and low-dispersion Runge-Kutta (LDDRK) scheme [37].

It must be emphasized that the above derivation does not impose any restrictions on the mean state $\overline{\mathbf{Q}}(\boldsymbol{x}, t)$, which can be spatially varying and temporally evolving. In a general implementation, a nonlinear solver is first used to obtain the mean state solution over the entire domain which is typically discretized using a nonuniform grid with coarse grid spacings in far-field regions. The mean state solution is then mapped onto the linear region which, as mentioned earlier, is discretized using a uniform

Cartesian mesh. The mean flow gradients must satisfy $\left|\nabla\overline{\mathbf{Q}}(\boldsymbol{x},t)\right| \ll 1$ in the linear region to ensure that the small perturbation assumption $|\mathbf{Q}'(\boldsymbol{x},t)| \ll \left|\overline{\mathbf{Q}}(\boldsymbol{x},t)\right|$ holds throughout the computation.

Temporally evolving mean states are to be globally updated by solving Eq. (6) with the instantaneous mean flux taken to be $\widehat{\mathrm{F}}_n^{ctr}(\overline{\mathbf{U}}_f)$. This is particularly convenient for multi-timescale problems where the mean state evolves slower in time compared to the perturbations. For such problems, it suffices to update the mean state over a much longer time step compared to the perturbations. In the present study, however, the mean state is uniform and steady in the linear region for simplicity. Hence, it was not necessary to update the mean states by solving Eq. (6).

2.2 Domain Decomposition Procedure

The advantage of decomposing the computational domain into multiple regions is the flexibility of solving different governing equations that best describe the flow physics in each region. For example, when solving for species concentrations in thermo-acoustic chemically reacting flows, chemical reactions and scalar transport must both be accounted for in the combustion zones while just the latter is sufficient in the far field. This added flexibility saves computational resources and can be used to adapt meshes in regions with need to do so. The general setup of the domain decomposition technique developed in the present study is shown in Figure 2. The Euler equations and its linearized counterpart are solved in the nonlinear and linear regions, respectively. Accurate two-way coupling between the regions is essential for the technique to work. This will be described in detail next.

2.2.1 Mapping from Nonlinear Region to Linear Region

As seen from Figure 2, the linear region overlaps the nonlinear region. The boundary of the nonlinear region that intersects the linear region is referred to as the overset boundary. Cells in the linear region that do not overlap the nonlinear region completely will be computed, i.e., $\mathbf{Q}_i'$ will be solved in these cells by computing the linearized fluxes at the cell faces. As for the cells that overlap the nonlinear region completely, it is sufficient to map three cells along each coordinate direction close to the overset boundary as illustrated in the cut-out of Figure 2. This is due to the symmetric six-cell stencil of the

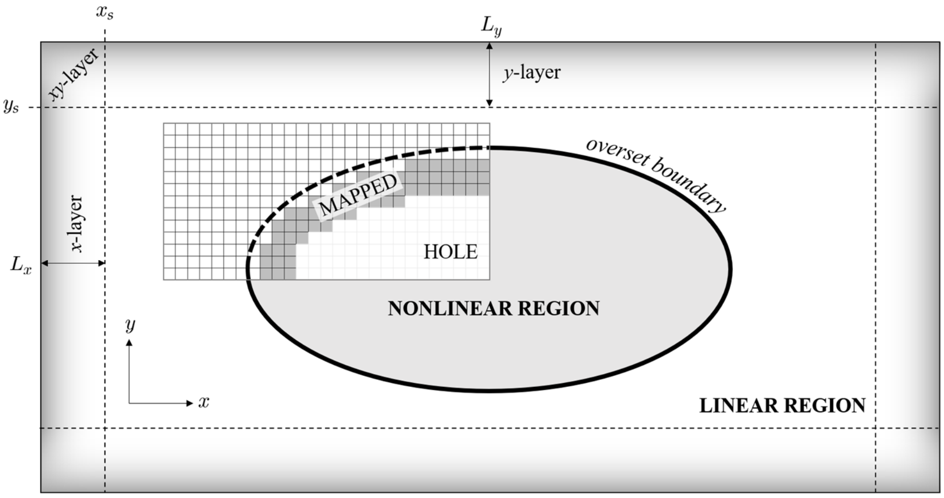

Figure 2: Schematic of domain decomposition setup for a general problem. Classification of linear region cells shown in cut-out.

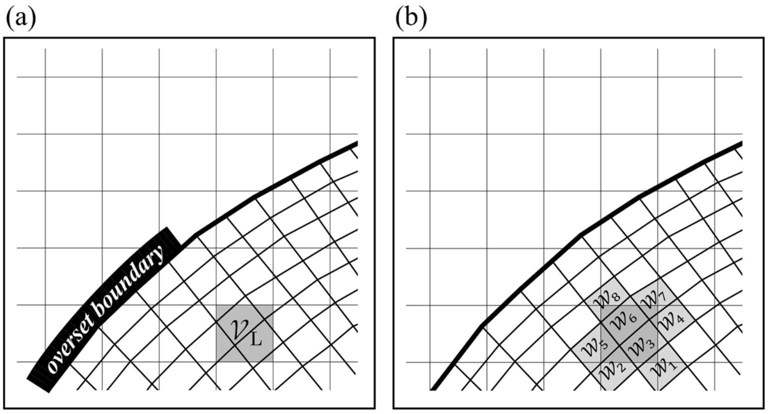

Figure 3: Volumetric mapping from nonlinear region to linear region.

DRP scheme utilized in the linear region (see Eq. (10)). Note that the mapped cells lie inside the nonlinear region completely. The remaining overlapping cells are treated as hole cells that are neither mapped nor computed.

Once a linear region cell $\mathcal{V}_\mathrm{L}$ has been marked for mapping (see Figure 3(a)), all the nonlinear region cells $\mathcal{W}_\mathrm{N}$ that overlap $\mathcal{V}_\mathrm{L}$ are first identified (see Figure 3(b)). Then, $\mathbf{Q}'_\mathrm{L}$ is determined as,

$$\mathbf{Q}'_\mathrm{L} = \left(\frac{1}{|\mathcal{V}_\mathrm{L}|} \sum_\mathrm{N} |\mathcal{V}_\mathrm{L} \cap \mathcal{W}_\mathrm{N}| \mathbf{Q}_\mathrm{N} \right) - \overline{\mathbf{Q}}_\mathrm{L}, \tag{14}$$

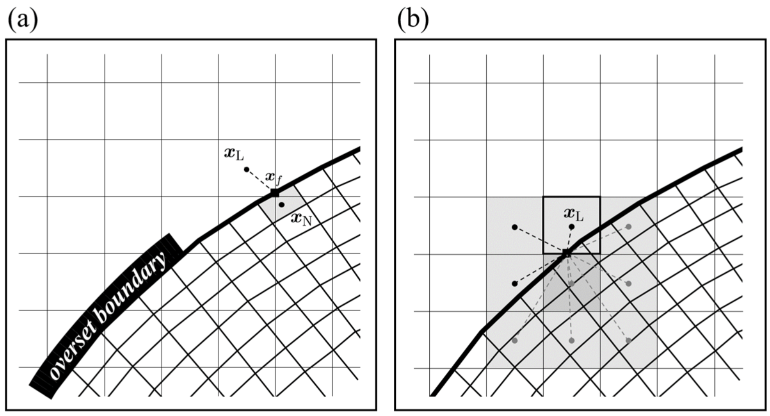

Figure 4: Linear interpolation at overset boundary faces.

whereby $|\mathcal{V}_\mathrm{L} \cap \mathcal{W}_\mathrm{N}|$ refers to the intersection volume of cells $\mathcal{V}_\mathrm{L}$ and $\mathcal{W}_\mathrm{N}$. For stationary meshes, the normalized intersection volumes $|\mathcal{V}_\mathrm{L} \cap \mathcal{W}_\mathrm{N}|/|\mathcal{V}_\mathrm{L}|$ can be computed once and stored at the start of the simulation. Note that the mean state $\overline{\mathbf{Q}}_\mathrm{L}$ is assumed to be known at all mapped cells in the linear region.

2.2.2 Mapping from Linear Region to Nonlinear Region

For the inverse mapping, a different approach is adopted. Since the nonlinear region utilizes second order schemes, it suffices to prescribe suitably interpolated primitive variables $\mathbf{U}_f$ at the face centroids of the overset boundary as a *boundary condition* to compute the central Euler fluxes (see Eq. (5)). Given a face centroid $\boldsymbol{x}_f$ on the overset boundary and its adjacent cell $\mathcal{W}_\mathrm{N}$ in the nonlinear region (shaded in Figure 4(a)), a suitable linear region cell $\mathcal{V}_\mathrm{L}$ must be determined to perform the linear interpolation,

$$\mathbf{U}_f = \frac{\|\boldsymbol{x}_f - \boldsymbol{x}_\mathrm{N}\|(\overline{\mathbf{U}}_\mathrm{L} + \mathbf{U}'_\mathrm{L}) + [(\boldsymbol{x}_\mathrm{L} - \boldsymbol{x}_f) \cdot \boldsymbol{d}_f]\mathbf{U}_\mathrm{N}}{(\boldsymbol{x}_\mathrm{L} - \boldsymbol{x}_\mathrm{N}) \cdot \boldsymbol{d}_f}, \qquad \boldsymbol{d}_f = \frac{\boldsymbol{x}_f - \boldsymbol{x}_\mathrm{N}}{\|\boldsymbol{x}_f - \boldsymbol{x}_\mathrm{N}\|}. \tag{15}$$

$\boldsymbol{x}_\mathrm{N}$ and $\boldsymbol{x}_\mathrm{L}$ refer to the centroids of cells $\mathcal{W}_\mathrm{N}$ and $\mathcal{V}_\mathrm{L}$, respectively. $\mathcal{V}_\mathrm{L}$ is chosen as the cell whose centroid $\boldsymbol{x}_\mathrm{L}$ lies the closest to the face centroid $\boldsymbol{x}_f$ as shown in Figure 4(a). If $\boldsymbol{x}_\mathrm{L}$ lies on the same side of the face as $\boldsymbol{x}_\mathrm{N}$, i.e. $(\boldsymbol{x}_\mathrm{L} - \boldsymbol{x}_f) \cdot \boldsymbol{d}_f < 0$, the interpolation weight becomes negative in Eq. (15). Such a scenario is depicted in Figure 4(b). To ensure positivity of interpolation weights, a different cell must be chosen. To this end, all cells in the linear region which share a vertex with the current $\mathcal{V}_\mathrm{L}$ are first identified. Ignoring cells whose centroids lie on the same side of the face as $\boldsymbol{x}_\mathrm{N}$ (cells with grey circles for centroids in Figure 4(b)), the cell with the closest centroid to $\boldsymbol{x}_f$ is chosen as $\mathcal{V}_{\mathrm{L}}$. In this scenario, this is the cell with the thick black border in Figure 4(b).

2.2.3 Sponge Layer Treatment

The linear region terminates in a sponge layer to prevent the reflection of acoustic waves back into the domain. The following dissipation term is added to the right-hand side of Eq. (7) in the sponge layers,

$$\mathrm{F}'_{sp} = \nabla \cdot (\omega(\boldsymbol{x}) \nabla \mathbf{Q}'). \tag{16}$$

where $\omega(\boldsymbol{x})$ represents an artificial viscosity. Applying the finite volume approximation, the numerical flux arising from the above dissipation term is given by,

$$\hat{\mathrm{F}}'_{sp,n} = \frac{1}{|\mathcal{V}_i|} \sum_{f \in \partial \mathcal{V}_i} \omega(\boldsymbol{x}_f) \left. \frac{\partial \mathbf{Q}'}{\partial n} \right|_{\boldsymbol{x}_f} S_f. \tag{17}$$

The derivative inside summation on the right-hand side is computed in the face normal direction $\boldsymbol{n}_f$. Denoting the neighbour cell of $\mathcal{V}_i$ adjacent to face f as $\mathcal{V}_j$, the derivative term can be approximated using the linear approximation scheme as,

$$\left. \frac{\partial \mathbf{Q}'}{\partial n} \right|_{\boldsymbol{x}_f} \approx \frac{\mathbf{Q}'_j - \mathbf{Q}'_i}{(\boldsymbol{x}_j - \boldsymbol{x}_i) \cdot \boldsymbol{n}_f}. \tag{18}$$

The artificial viscosity $\omega(\boldsymbol{x})$ is defined as follows in the x- and y-layers (see Figure 2), respectively.

$$\omega_x(\boldsymbol{x}) = \omega_{max} \left(\frac{x - x_s}{L_x} \right)^2 \frac{(\Delta x)^2}{\Delta t}, \qquad \omega_y(\boldsymbol{x}) = \omega_{max} \left(\frac{y - y_s}{L_y} \right)^2 \frac{(\Delta y)^2}{\Delta t}. \tag{19}$$

L_x and L_y refer to the sponge layer lengths and, x_s and y_s refer to the sponge layer starting locations. Δx and Δy refer to the cell size in the linear region and Δt refers to the time step. As the linear region is discretized using a uniform Cartesian mesh, $\Delta x = \Delta y$ is the same at all faces. ω_{max} is a non-dimensional parameter defined by the user for controlling the maximum viscosity at the end of the sponge layers. Therefore, the above definition adjusts the amplitude of ω based on the spatial and temporal resolutions. Currently, the *xy*-layers at the corners are treated as superpositions of the respective *x*- and *y*-layers, i.e., $\omega_{xy}(\boldsymbol{x}) = \omega_x(\boldsymbol{x}) + \omega_y(\boldsymbol{x})$.

3 Numerical Results

For all test cases presented, the primitive variable perturbations $\mathbf{U}'$ were used to initialize the linear region; the conserved variable perturbations $\mathbf{Q}'$ were initialized using Eqs. (12) and (13). The initial conditions for the perturbations are given by the following Gaussian function,

$$\mathrm{G}(x; x_0, w) = \exp\left[-\ln 2\left(\frac{x - x_0}{w}\right)^2\right]. \tag{20}$$

Parameters x_0 and w refer to the centre location and half-width of the Gaussian profile, respectively.

3.1 Validation of Linear Solver

Prior to investigating the domain decomposition technique, the finite volume formulation of the linearized Euler fluxes computed using the DRP interpolation scheme must be validated. The validation test case was initialized with an acoustic pulse and an entropy wave as given below.

$$\begin{aligned} p'(x,0) &= 10^{-2}\mathrm{G}(x; 0{,}3), \\ u'(x,0) &= 0, \\ \rho'(x,0) &= 10^{-2}\mathrm{G}(x; 0{,}3) + 10^{-3}\mathrm{G}\left(x; \tfrac{200}{3}, 5\right) \end{aligned} \tag{21}$$

The mean state given below is a uniform flow with Mach number $M = 0.5$:

$$\bar{p}(x,t) = 1, \qquad \bar{u}(x,t) = 0.5, \qquad \bar{\rho}(x,t) = 1.4. \tag{22}$$

The computational domain $x \in [-150{,}150]$ was discretized into uniform cells of width $\Delta x = 1$. The regions $x \in [-150, -100]$ and $x \in [100{,}150]$ were treated as sponge (*x*-)layers with $L_x = 50$ and $\omega_{max} = 0.0025$. The choice of values for L_x and ω_{max} was obtained from numerical testing by

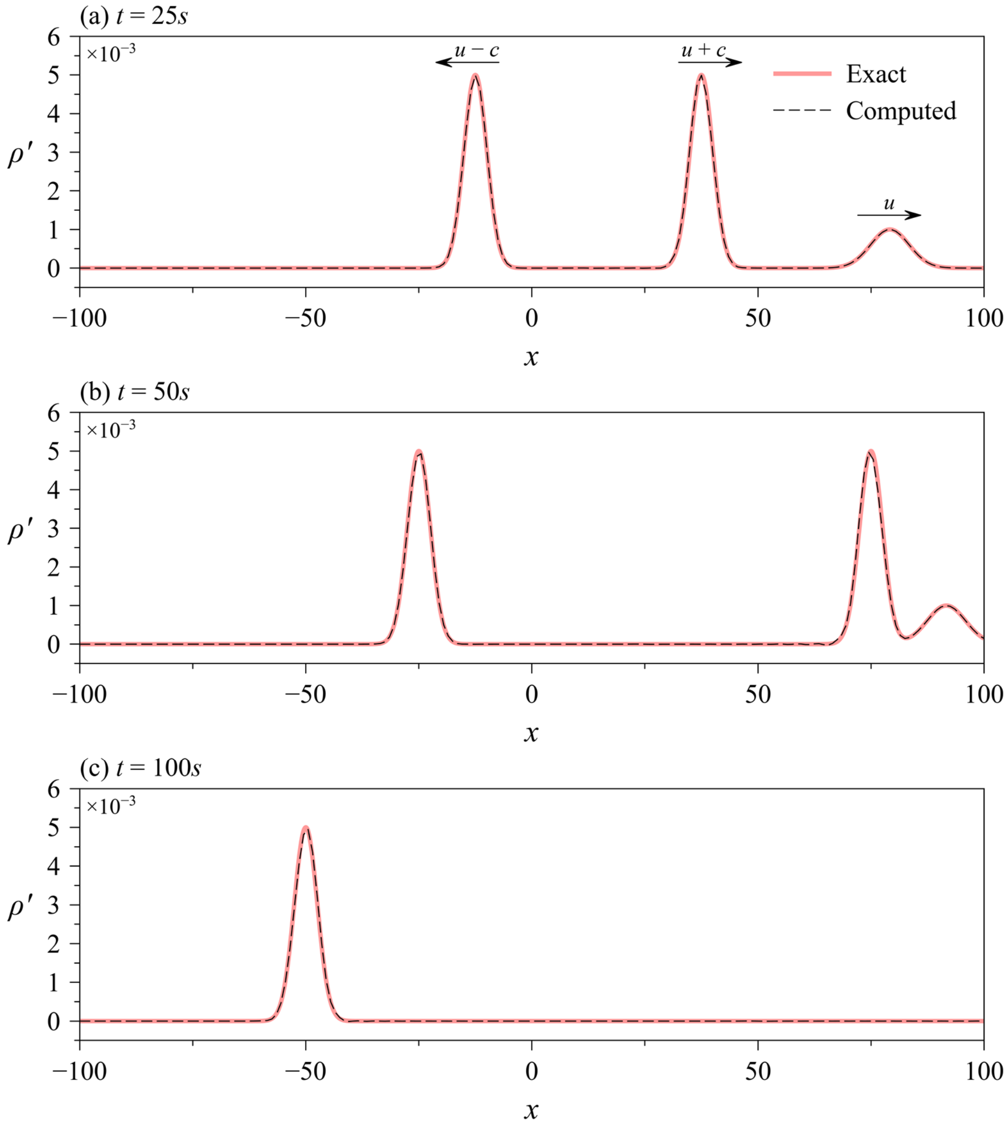

Figure 5: Comparison of computed results with the exact solution for linear solver validation case.

Table 1: L_∞ norm of ρ' for linear solver validation case at different times.

t	$25s$	$50s$	$75s$	$100s$
$\max\limits_i \lvert \rho'_i - \rho'_{i,exact} \rvert$	$1.3111e{-4}$	$2.4247e{-4}$	$1.2568e{-4}$	$1.5398e{-4}$

requiring that the acoustic waves fully decay at the outer edge of the boundary with no reflections into the domain. These values were used for the remaining simulations in this paper.

Upon initialization, the acoustic pulse splits into two acoustic waves, one moving to the right at a speed of $\bar{u} + \bar{c} = 1.5$ and the other moving to the left at a speed of $\bar{u} - \bar{c} = -0.5$. The entropy wave moves to the right at the flow velocity $\bar{u} = 0.5$. At $t \approx 66.7s$, the right-going acoustic and entropy wave reach

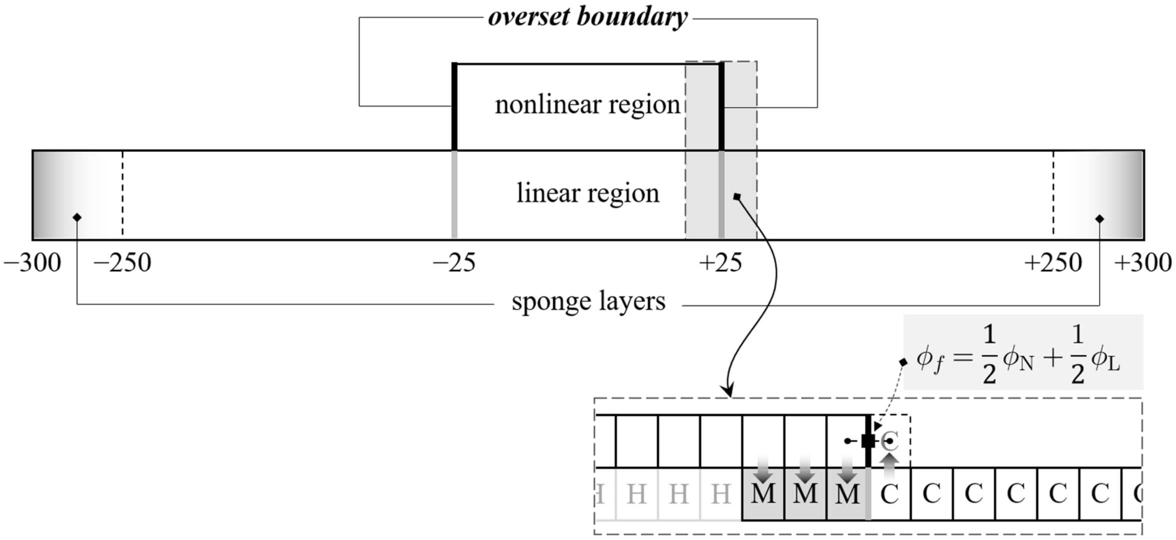

Figure 6: Schematic of domain decomposition setup in 1D for validation case.

the starting location of the right sponge layer $x_s = 100$ simultaneously. The problem was computed until $t = 100s$ with a time step of $\Delta t = 0.05s$. $\rho'(x,t)$ at $t = 25$, 50 and $100s$ are compared with the exact solution in Figure 5. It can be seen that the results agree well with the exact solution. To have a better representation of the numerical errors, the maximum absolute difference between the exact and computed solutions are listed in Table 1 at four time instants. The drop in error from $t = 50s$ to $t = 75s$ occurs due to the right-going acoustic wave and entropy wave moving beyond $x = 100$ where they get dampened by the right sponge layer. The results also demonstrate that the sponge layer is effective in preventing the reflection of waves back into the domain.

3.2 Validation of Domain Decomposition

Before addressing the interaction of waves with shock waves, the domain decomposition technique is validated. A schematic of the one-dimensional domain decomposition setup for the validation test case is shown in Figure 6. The nonlinear region is drawn above the linear region in the schematic for clarity. The nonlinear region lies between $x \in [-25,25]$ and terminates with the overset boundary. The linear region lies between $x \in [-300,300]$ and terminates in sponge layers of lengths $L_x = 50$. A close-up view near the right overset boundary is shown in the schematic to illustrate the coupling procedure between the regions. The letters ‘C’, ‘M’ and ‘H’ refer to computed, mapped and hole cells, respectively. The thick arrows indicate the transfer of information from one region to the other. For the validation case, both regions were discretized uniformly into cells of width $\Delta x = 1$. Therefore, three nonlinear region cells next to the overset boundary are directly mapped to the three mapped cells (M) in the linear region. On the other hand, the first computed cell (C) next to the mapped cell in the linear region and the nonlinear region cell immediately adjacent to the overset boundary are used in the interpolation at the overset boundary. The situation is identical at the left overset boundary.

The test case was initialized with a right-travelling acoustic wave at $x = -165$, a left-travelling acoustic wave at $x = 55$ and an entropy wave at $x = -55$ as follows:

$$\begin{aligned} p'(x,0) &= \epsilon[0.5\mathrm{G}(x; -165{,}12) + \mathrm{G}(x; 55{,}8)], \\ u'(x,0) &= \epsilon\left[\tfrac{0.5}{1.4}\mathrm{G}(x; -165{,}12) - \tfrac{1.0}{1.4}\mathrm{G}(x; ,55{,}8)\right], \\ \rho'(x,0) &= \epsilon[0.5\mathrm{G}(x; -165{,}12) + \mathrm{G}(x; 55{,}8) - 0.5\mathrm{G}(x; -55{,}8)]. \end{aligned} \tag{23}$$

The problem was computed for two perturbation amplitudes $\epsilon = 10^{-2}$ and $\epsilon = 10^{-5}$. The mean state in the linear region is the same as that given in Eq. (22). The nonlinear region was initialized with the same state. The problem was computed up to $t = 220s$ using a timestep of $\Delta t = 0.05s$. Upon initialization, all three waves move into the nonlinear region and intersect with each other before re-emerging on the opposite side of the linear region. $\rho'(x,t)$ for $\epsilon = 10^{-2}$ at $t =$ 55, 110, 165 and $220s$ are compared with the exact solution in Figure 7. The results agree well with the exact solution. At $t = 220s$ (see Figure 7(d)), a slight phase shift can be observed for the right-travelling acoustic wave and the entropy wave. This is most likely a consequence of the dispersion error incurred in the nonlinear region due to the use of second order schemes. The results for $\epsilon = 10^{-5}$ were qualitatively similar. The effect of using smaller cells in the nonlinear region will be investigated in the next section.

Though the linear and nonlinear solvers are inherently conservative within the respective regions, conservation is not preserved exactly at the overset boundary. To determine the conservation error incurred, the total energy perturbation $(\rho e_t)'$ was integrated over both regions at each timestep. The integrated values $E(t) \equiv \int (\rho e_t)'(t)\ dV$, normalized by the initial value $E(0)$, are plotted in Figure 8

(a) $t = 55s$

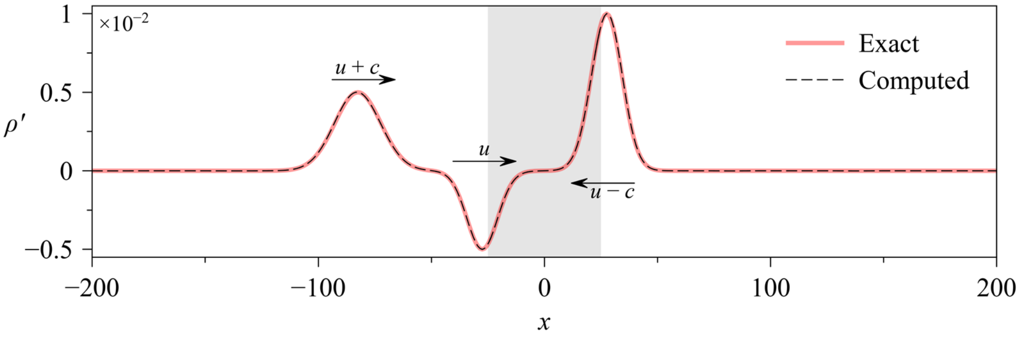

(b) $t = 110s$

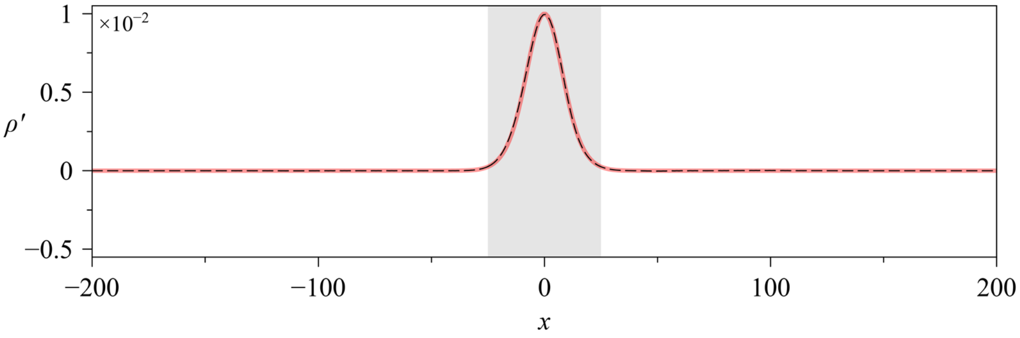

(c) $t = 165s$

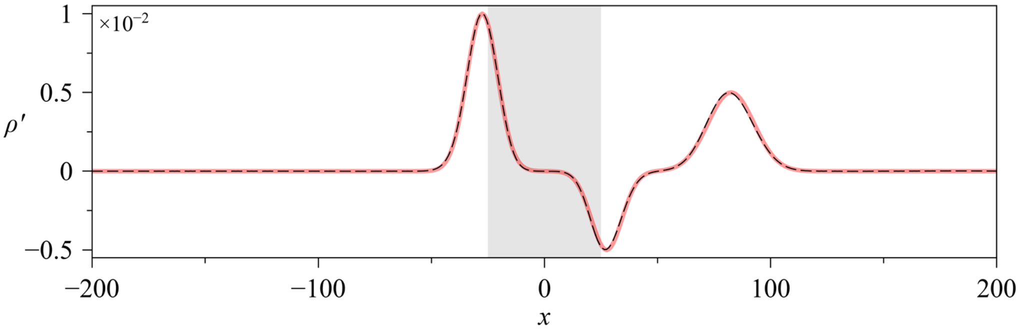

(d) $t = 220s$

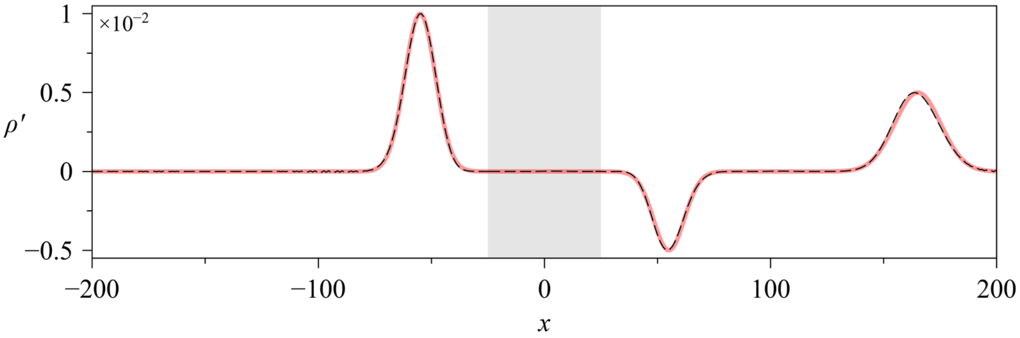

Figure 7: Comparison of computed results with the exact solution for domain decomposition validation case with $\epsilon = 10^{-2}$. Nonlinear region is shaded grey.

for $\epsilon = 10^{-5}$ and $\epsilon = 10^{-2}$. It can be observed that $E(t)/E(0) \approx 1$ throughout the computation for both values of ϵ. The maximum deviation in $E(t)/E(0)$ is 0.02% for $\epsilon = 10^{-5}$ and 0.8% for $\epsilon = 10^{-2}$.

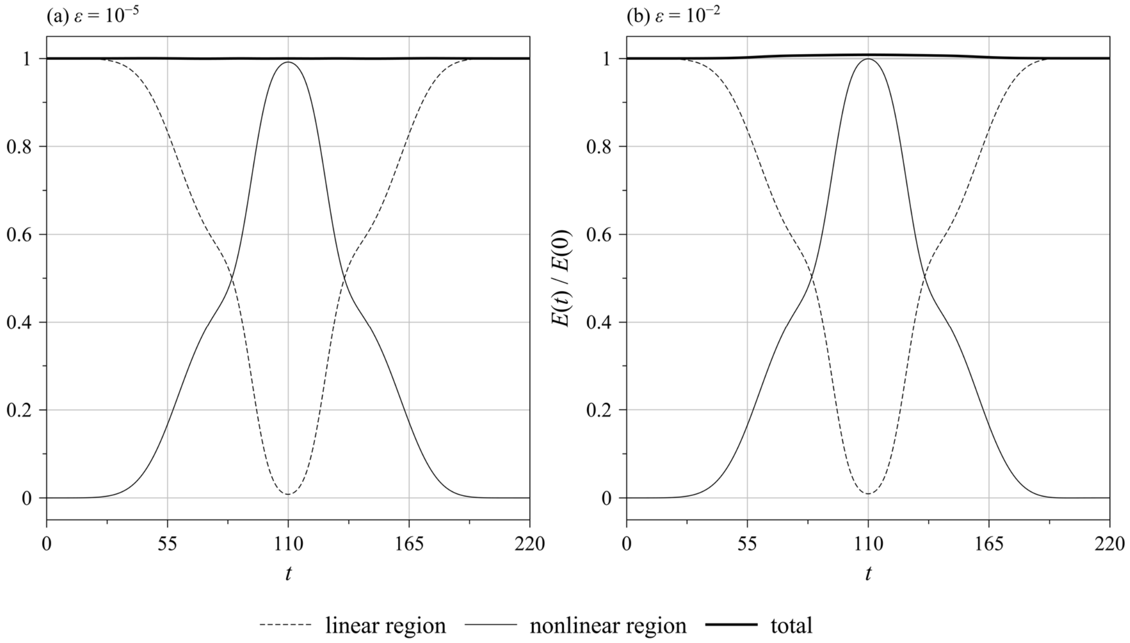

Figure 8: Time variation of normalized integrated total energy perturbation for domain decomposition validation case.

3.2.1 Effect of Cell Size Ratio

For the shock-acoustic/entropy wave interaction problem, a finer mesh is required in the nonlinear region to capture the shock motion accurately whereas a coarser mesh can be utilized in the linear region for the wave propagation. The effect of different cell size ratios for the linear and nonlinear regions will be investigated in this section. In this investigation, both regions were discretized uniformly but with cells of different widths. The cell size ratio R is defined as $\Delta x_{\mathrm{L}}/\Delta x_{\mathrm{N}}$. The test case involves the propagation of a single right-travelling acoustic wave in stationary flow. The acoustic wave was initialized as,

$$\begin{aligned} p'(x,0) &= \epsilon \mathrm{G}(x;-65{,}6), \\ u'(x,0) &= \tfrac{\epsilon}{1.4}\mathrm{G}(x;-65{,}6), \\ \rho'(x,0) &= \epsilon \mathrm{G}(x;-65{,}6). \end{aligned} \tag{24}$$

ϵ was set to 10^{-5}. The mean state in the linear region and the nonlinear region were initialized as follows:

$$\bar{p}(x,t) = p(x,0) = 1, \qquad \bar{u}(x,t) = u(x,0) = 0, \qquad \bar{\rho}(x,t) = \rho(x,0) = 1.4. \tag{25}$$

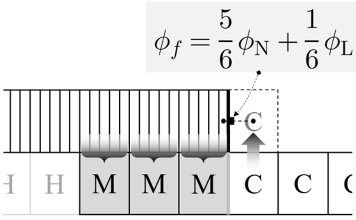

Figure 9: Close-up view near right overset boundary for cell size ratio $R = 5$. Nonlinear region is positioned above the linear region.

The linear region extends between $x \in [-100{,}100]$ while the nonlinear region extends between $x \in [-25{,}25]$. Instead of sponge layers, periodic boundary conditions were applied at the ends of the linear region so that the acoustic wave re-enters the linear region from the left boundary as it exits through the right boundary. The periodic boundary condition simulates the effect of the acoustic waves propagating over long distances, which is the common case in aeroacoustic simulations performed to predict far-field noise. The problem was computed with CFL $= 0.5$ until the acoustic wave returns to its initial location after 10 cycles at $t = 2000$s. The computation was performed for $R = 1, 2, 5$, and 10. A close-up view near the right overset boundary for $R = 5$ is shown in Figure 9. Notice the change in interpolation weights for the overset boundary face compared to $R = 1$ shown earlier in Figure 6.

Baseline computations using a linear solver and a nonlinear solver were also performed. For these runs, the periodic computational domain $x \in [-100{,}100]$ consisted of a single region that was discretized uniformly. The linear computation was performed for $\Delta x_{\mathrm{L}} = 1$, whereas the nonlinear computations were performed for $\Delta x_{\mathrm{N}} = 1, 0.5, 0.2$, and 0.1 which correspond to the nonlinear cell spacings used at cell size ratios $R = 1, 2, 5$ and 10, respectively, for the domain decomposition computations.

$\rho'(x, t)$ at $t = 200s$ are plotted in Figure 10 for selected cases. Figure 10(a) shows that the final result from the linear computation for $\Delta x_{\mathrm{L}} = 1$ is indistinguishable from the exact solution. Figure 10(b) show that the nonlinear computations for the coarsest mesh resolution $\Delta x_{\mathrm{N}} = 1$ results in a noticeable phase shift as well as a larger undershoot near $x = -80$. Both discrepancies are significantly reduced at the finest mesh resolution $\Delta x_{\mathrm{N}} = 0.1$. In contrast, Figure 10(c) shows that the domain decomposition

(a) Purely linear

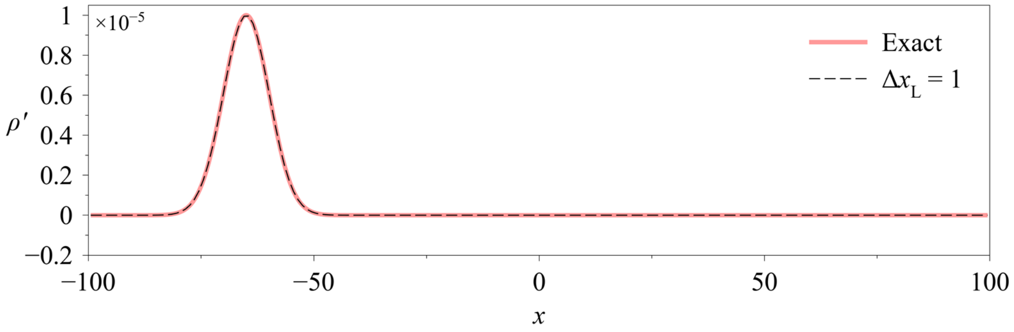

(b) Purely nonlinear

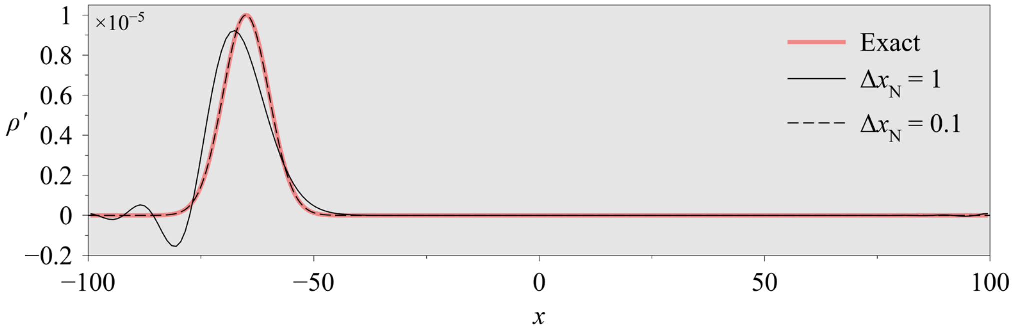

(c) Domain decomposition

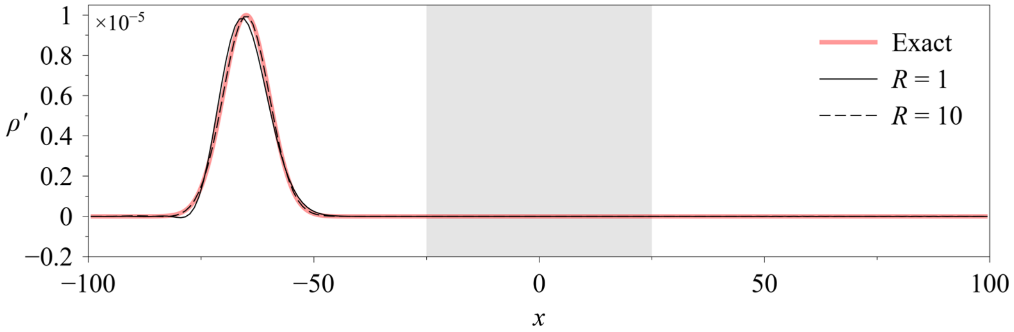

Figure 10: Results for propagation of a single acoustic wave at $t = 200s$

computations at $R = 1$ significantly reduce the phase shift and undershoot observed in Figure 10(b) for $\Delta x_{\mathrm{N}} = 1$. At $R = 10$, the domain decomposition results become nearly identical to the exact solution.

The average density perturbation error $\widehat{\rho'}$ is defined by,

$$\widehat{\rho'} = \int |\rho' - \rho'_{exact}|\, dV \Big/ \int dV. \tag{26}$$

It can be seen from Figure 11 that $\widehat{\rho'}$ grows in time for all cases, which is expected since both the dispersion and dissipation errors accumulate as the wave propagates through larger distances. The linear solver produces the smallest error among all the runs due to the significantly smaller dispersion errors incurred by the DRP scheme. In contrast, much larger errors are produced by the nonlinear computations

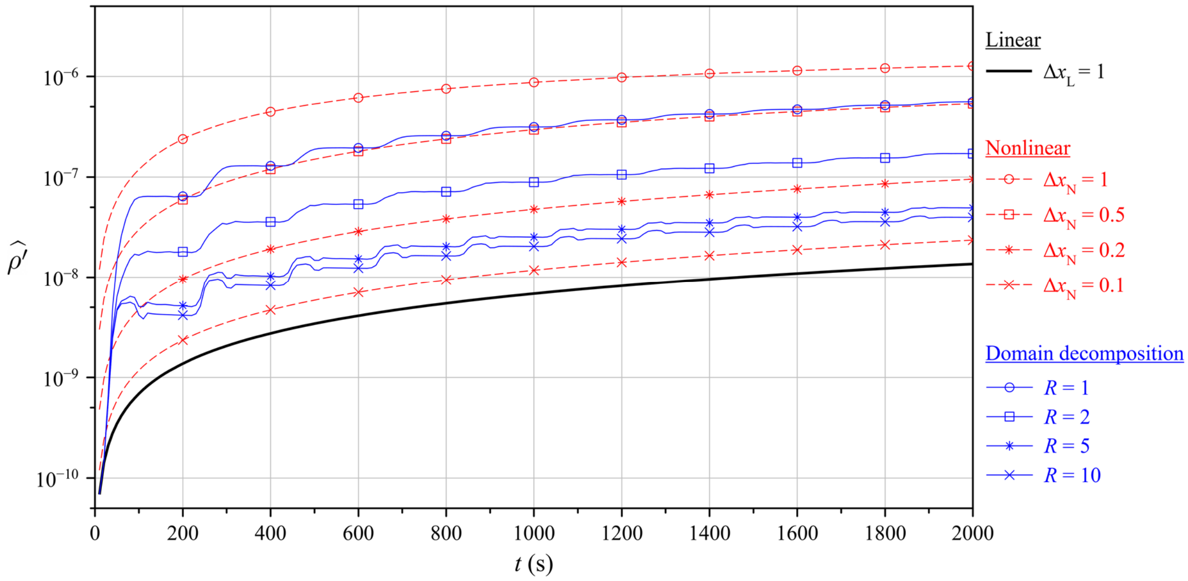

Figure 11: Average density errors versus time for different types of computations at various mesh resolutions/cell size ratios for propagation of a single acoustic wave.

due to the poor dispersion properties of the second order linear interpolation schemes. For the same mesh resolution $\Delta x_{\mathrm{L}} = \Delta x_{\mathrm{N}} = 1$, $\widehat{\rho'}$ is two orders larger for the nonlinear computation compared to the linear computation. Though the errors reduce with mesh resolution, even at ten times the refinement, the nonlinear computation for $\Delta x_{\mathrm{N}} = 0.1$ is still worse than the linear computation for $\Delta x_{\mathrm{L}} = 1$. Similar to the nonlinear computations, the errors incurred by the domain decomposition technique are always greater than the error incurred by the linear solver. The coupling procedure in the domain decomposition introduces additional errors to the discretization errors in the linear and nonlinear regions separately. The coupling error is evident from the periodic bumps seen in Figure 11 for the domain decomposition technique, which are produced when the acoustic wave crosses coupling zones. While increasing cell size ratio R reduces the numerical error as expected, the reduction becomes increasingly less significant at higher values of R. With $R = 1$, the error incurred by the domain decomposition technique is close to that of the nonlinear computation with $\Delta x_{\mathrm{N}} = 0.5$. It can be seen from Figure 11 that doubling the cell size ratio from $R = 1$ to $R = 2$ produced a greater reduction in error compared to the doubling from $R = 5$ to $R = 10$. In contrast, for the nonlinear computations, doubling the mesh refinement from $\Delta x_{\mathrm{N}} = 1$ to $\Delta x_{\mathrm{N}} = 0.5$ produced roughly the same reduction in error as doubling it from $\Delta x_{\mathrm{N}} = 0.2$ to $\Delta x_{\mathrm{N}} = 0.1$. For this reason, the domain decomposition case at $R = 10$, unlike the

Table 2: Relative wall times for different types of computations at various mesh resolutions/cell size ratios for propagation of a single acoustic wave.

Type of computation	Mesh	Δt	Relative wall time
Linear	$\Delta x_{\mathrm{L}} = 1$	0.50	1.00
Nonlinear	$\Delta x_{\mathrm{N}} = 1$	0.50	1.29
	$\Delta x_{\mathrm{N}} = 0.5$	0.25	3.29
	$\Delta x_{\mathrm{N}} = 0.2$	0.10	13.57
	$\Delta x_{\mathrm{N}} = 0.1$	0.05	43.71
Domain decomposition	$R = 1$	0.50	1.14
	$R = 2$	0.25	2.71
	$R = 5$	0.10	8.14
	$R = 10$	0.05	20.14

other cell size ratios, actually performs worse than the nonlinear case at $\Delta x_{\mathrm{N}} = 0.1$. The saturated performance of the domain decomposition technique is attributed to the increasingly significant coupling errors, suggesting that there is no advantage to be gained by increasing R any further. However, the coupling errors can be reduced to a great extent when high-order interpolation is used at the overset boundary (see Section 3.4.2), potentially permitting larger values of R.

The relative wall times for the various computations are listed in Table 2. It can be seen that the linear computation has the least wall time. The nonlinear computation takes slightly longer than the linear computation for the same mesh resolution of $\Delta x_{\mathrm{L}} = \Delta x_{\mathrm{N}} = 1$, most likely due to the greater computational cost of hybrid central-upwind flux scheme compared to the linearized fluxes. The domain decomposition computations take shorter times than the nonlinear computations for the corresponding Δx_{N}. The wall times for the nonlinear and domain decomposition computations increase with mesh refinement due to the greater number of cells and the reduction in time step in accordance with CFL. However, the wall times increase at a much slower rate for the domain decomposition technique, giving it an attractive computational advantage. For instance, Figure 11 shows that the purely nonlinear computation for $\Delta x_{\mathrm{N}} = 0.5$ and the domain decomposition technique for $R = 1$ are comparable in accuracy. Yet, comparing their wall times in Table 2 shows that the latter is nearly three times faster. The relative speedups given in Table 2 are specific to an occupancy ratio of 25%, i.e., the nonlinear region occupies 25% of the linear region. Computations performed at various occupancy ratios showed that the computational time increases linearly with the occupancy ratio.

Based on the discussion thus far, it can be concluded that linear computation should be used wherever propagation of only linear waves is to be considered. However, when nonlinear effects need to be accounted for in a localized region, it is more effective to use the domain decomposition technique than nonlinear computation. The domain decomposition technique reduces the overall cell count, resulting in faster computation times without sacrificing accuracy.

3.3 Case Study: Interaction of an Acoustic/Entropy Wave with a Standing Shock Wave

In this section, the domain decomposition technique is applied to study the interaction of an acoustic/entropy wave with a shock wave. In one-dimensional uniform mean flow, there exist three types of linear waves – two acoustic waves propagating at speeds $u \pm c$ and an entropy wave travelling at u. For conciseness, the waves will be referred by their wave speeds henceforth. A normal shock wave is a discontinuity separating two uniform mean states. Thus, there may exist six linear waves, three on either side of the shock. A steady shock wave is shown with supersonic flow on its left and subsonic flow on its right in Figure 12. Quantities on the supersonic (left) and subsonic (right) sides are denoted with subscripts 'l' and 'r', respectively. Since the flow is supersonic on the left, all three types of waves ($u_l \pm c_l, u_l$) approach the shock from the left and interact with it (see Figure 12(a)). The interaction causes the shock wave to move left or right while, simultaneously, generating an acoustic $u_r + c_r$ wave and an entropy u_r wave, both of which travel downstream to the right (see Figure 12(b)). Note that only these two wave types can propagate away from the standing shock, so no other wave type is generated by the current interaction. For small amplitudes, the generated waves have the same profile as the incoming ones, which is a Gaussian in the present study. The amplitudes of the generated waves and the shock velocity can be approximated by the linearized interaction analysis (LIA). A simplified derivation of the LIA performed by Moore [9] is provided in the Appendix A1.

Due to the discontinuous nature of the mean flow and shift in shock wave position during the interaction, it is not possible to compute this problem using a linear solver. The domain decomposition technique

(a) Before interaction

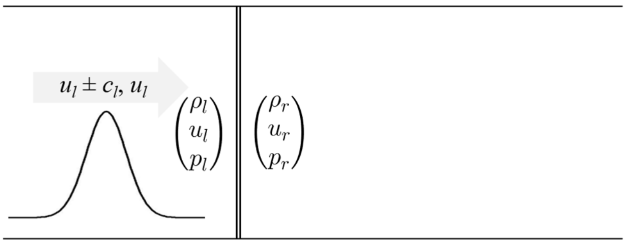

(b) After interaction

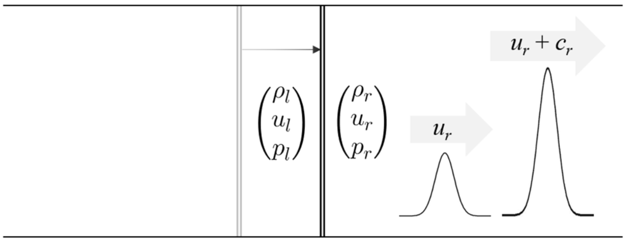

Figure 12: Schematic of shock interaction with an acoustic/entropy wave.

is most suitable for this application as it accounts for the localized nonlinear effects while maintaining computational efficiency and accuracy for the propagation of small disturbances in the far field. For this problem, the linear region extends between $x \in [-150{,}150]$ and terminate in sponge layers of lengths $L_x = 50$ at either ends. The nonlinear region extends between $x \in [-5{,}5]$. The linear region was discretized uniformly with $\Delta x_{\mathrm{L}} = 1$ as in the previous cases. The nonlinear region, however, was discretized non-uniformly. The nonlinear region cells that map onto the linear region cells were of a uniform width $\Delta x_{\mathrm{N}} = 0.1$, resulting in a cell size ratio of $R = 10$ in the range $2 < |x| < 5$. Beyond that, the cell size was refined geometrically from both sides in a symmetric manner until a minimum cell width of $\Delta x_{\mathrm{N}} = 0.001$ was achieved at $x = 0$.

Each case was initialized with a standing shock wave at $x = 0$. The nonlinear region and the mean state in the linear region were initialized as follows using normal shock relationships based on the Mach number, M, on the supersonic side (i.e., $M > 1$):

$$\begin{gathered}
\bar{p}(x,t) = p(x,0) = \begin{cases} 1, & x < 0 \\ \dfrac{2\gamma M^2 - \gamma + 1}{\gamma + 1}, & x > 0 \end{cases}, \\
\bar{u}(x,t) = u(x.0) = \begin{cases} M, & x < 0 \\ \dfrac{(\gamma - 1)M^2 + 2}{(\gamma + 1)M}, & x > 0 \end{cases},
\end{gathered} \tag{27}$$

$$\bar{\rho}(x,t) = \rho(x.0) = \begin{cases} 1.4, & x < 0 \\ \dfrac{1.4(\gamma+1)M^2}{(\gamma-1)M^2+2}, & x > 0 \end{cases}.$$

The $u_l \pm c_l$ waves were initialized as follows.

$$\begin{aligned} p'(x,0) &= \epsilon \mathrm{G}(x; -50{,}12), \\ u'(x,0) &= \pm \tfrac{\epsilon}{1.4} \mathrm{G}(x; -50{,}12), \\ \rho'(x,0) &= \epsilon \mathrm{G}(x; -50{,}12). \end{aligned} \tag{28}$$

For the u_l wave, ρ' was initialized as above while p' and u' were set to zero. The three wave types were investigated for three Mach numbers $M = 1.5$, 3, and 5. Each wave type/Mach number combination was computed four times with $\epsilon = \pm 10^{-2}$ and $\pm 10^{-5}$.

p' and ρ' profiles from the linear region are plotted in Figure 13 for the interaction of a $u_l + c_l$ wave of amplitude $\epsilon = 10^{-2}$ with a $M = 3$ shock wave. As the incoming wave interacts with the shock wave, two new waves are the generated on the subsonic side: a $u_r + c_r$ wave and a u_r wave. Both these waves travel away from the shock to the right. The u_r wave trailing behind the $u_r + c_r$ wave is clearly distinguishable in Figure 13(d) by the presence of density perturbation without any pressure perturbation. The time variation of the normalized integrated total energy $E(t)/E(0)$ is plotted in Figure 14 for this case. It can be seen that there is an exchange of energy between the regions at the end of the interaction while the total energy is conserved throughout the interaction. The results are qualitatively similar for the other two wave types, $u_l - c_l$ and u_l. The relative amplitude of the $u_r + c_r$ wave generated can be quantified by the parameter $\max(p'/\epsilon)$. It can be seen from Figure 13(d) that $\max(p'/\epsilon) \approx 7$. The results for the interaction of shock waves with all three types of waves approaching the shock from the supersonic side are plotted in Figure 15 in terms of $\max(p'/\epsilon)$. Estimations from LIA are also included for comparison.

The results agree well with the theoretical predictions for $|\epsilon| = 10^{-2}$. For $|\epsilon| = 10^{-5}$, however, the results not only deviate from theoretical predictions, but they do so asymmetrically, depending on the sign of ϵ. The deviations also become larger as the Mach number increases. This is a counterintuitive

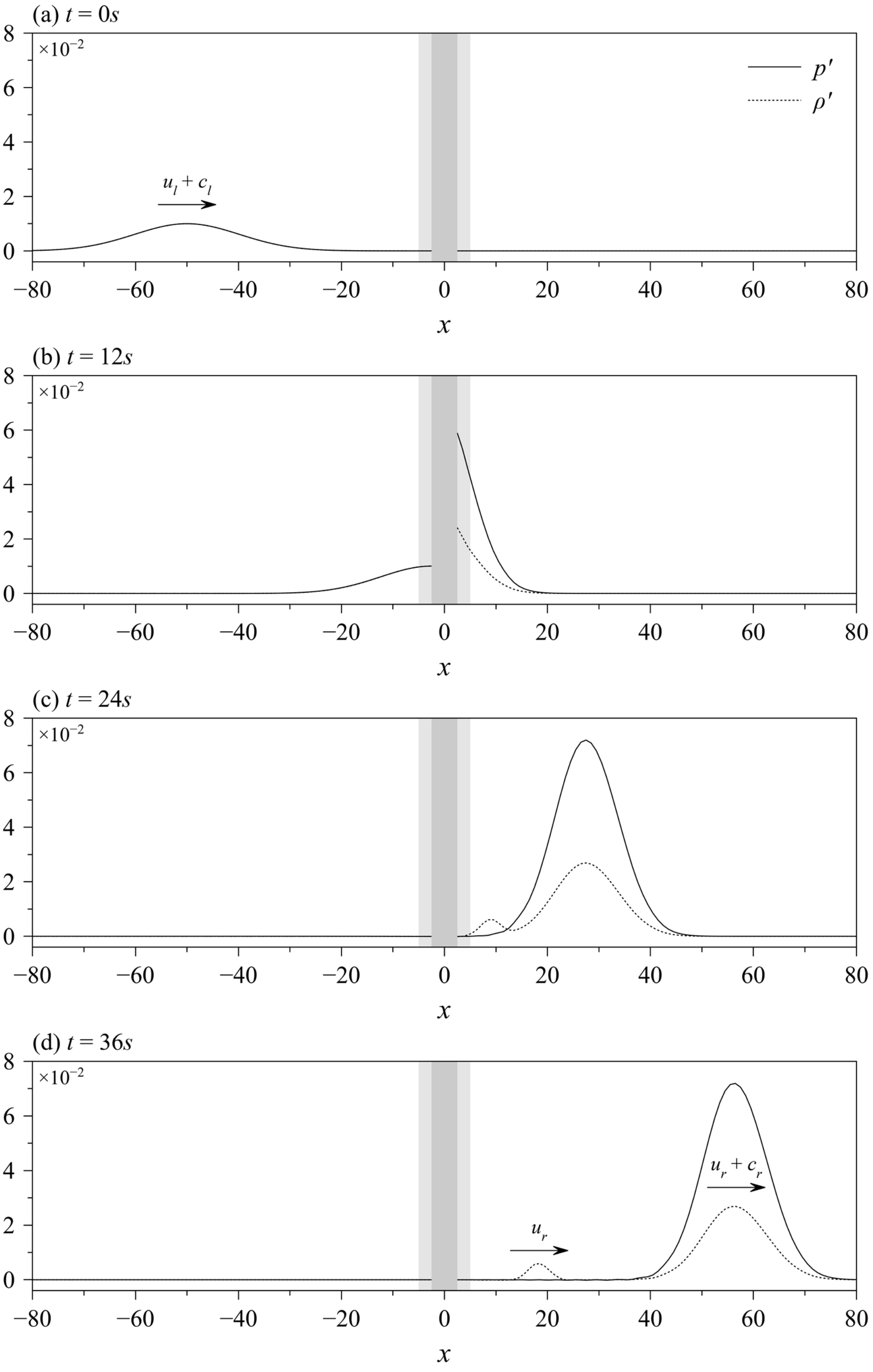

Figure 13: Interaction of a $u_l + c_l$ acoustic wave with a $M = 3$ standing shock for $\epsilon = 10^{-2}$.

behaviour as one would expect a closer agreement with LIA for smaller perturbations. To determine whether this behaviour is unique to the HLLC scheme, the computations were repeated with HLLE [38]

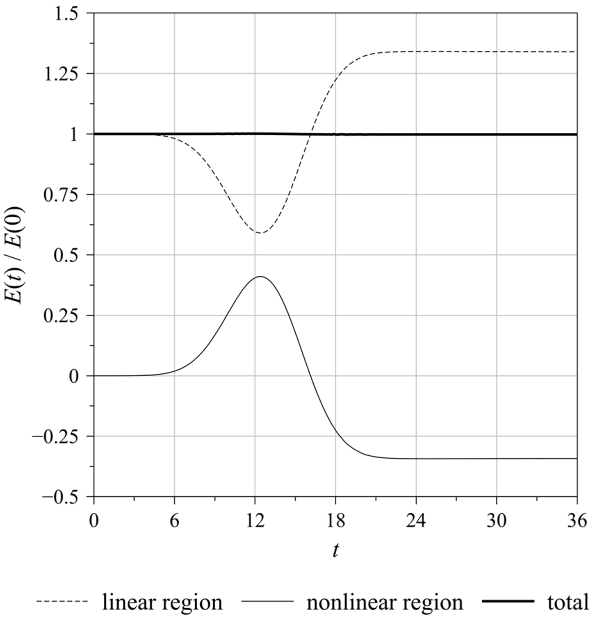

Figure 14: Time variation of normalized integrated total energy perturbation for $M = 3$ shock interaction with a $u_l + c_l$ wave of amplitude $\epsilon = 10^{-2}$.

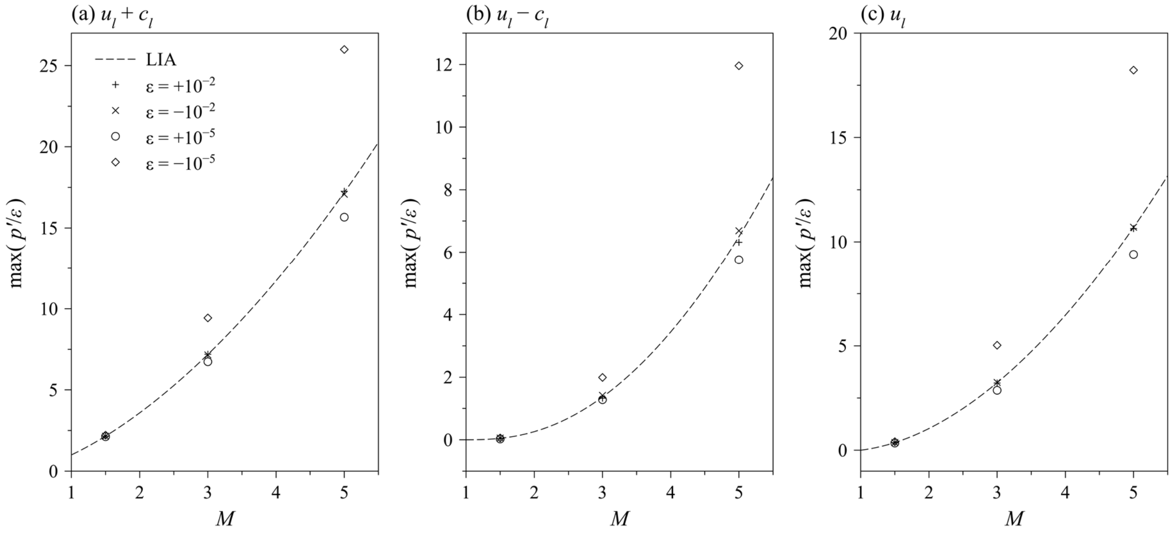

Figure 15: Relative amplitudes of $u_r + c_r$ acoustic wave generated by interaction of different types of waves interacting with the shock.

and Roe [39] schemes, both demonstrating similar trends. Therefore, the deviation is not caused by the choice of the upwind flux scheme.

To better understand the mechanism behind this behaviour and its dependence on mesh resolution, the case of a $M = 3$ shock interacting with a $u_l + c_l$ wave of amplitude $\epsilon = 10^{-2}$ was computed on a very

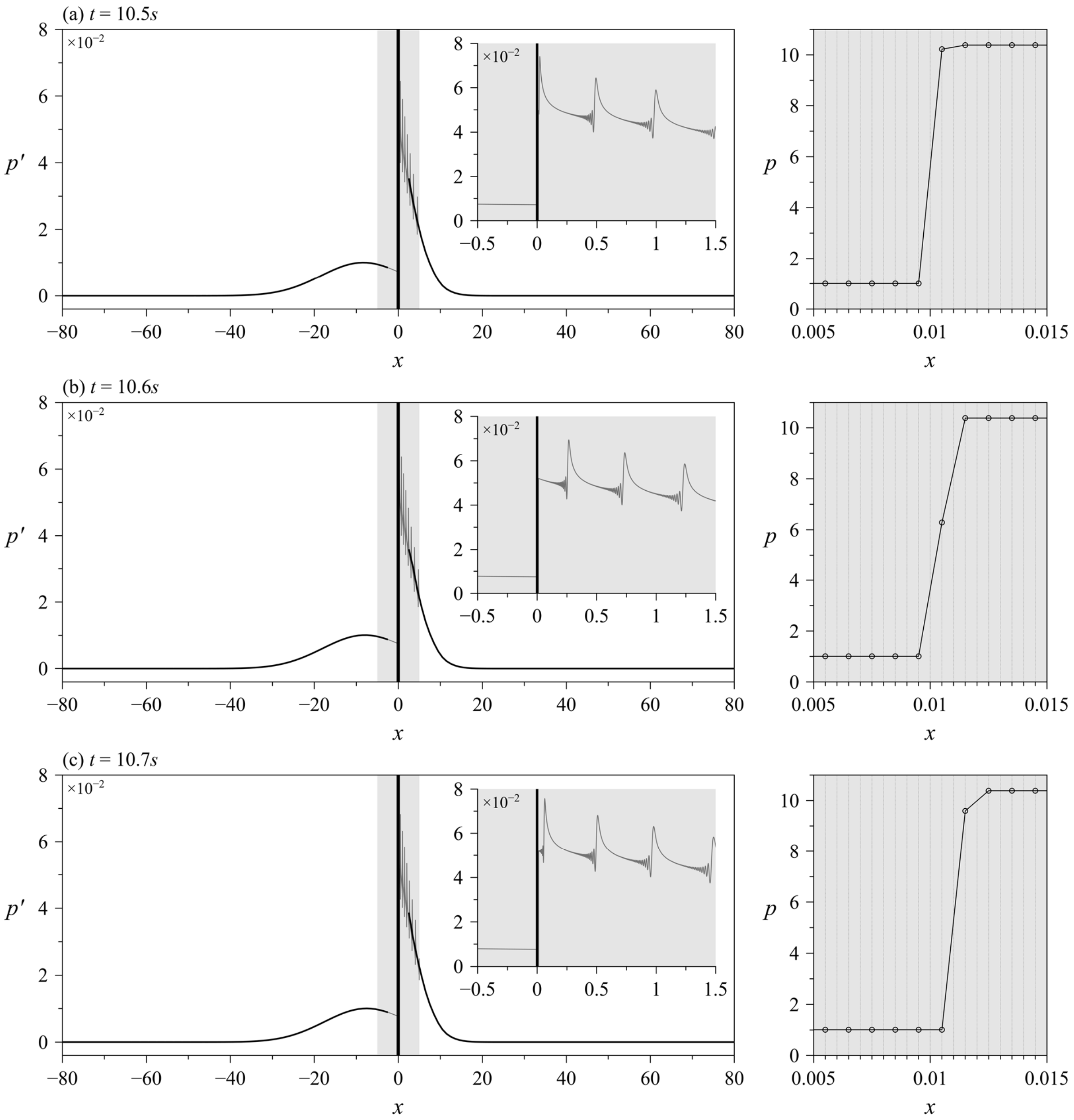

Figure 16: Pressure perturbations generated for the case of a $M = 3$ shock interacting with a $u_l + c_l$ wave of amplitude $\epsilon = 10^{-2}$ as the shock crosses one cell in the nonlinear region.

fine mesh (uniform cell spacing of $\Delta x_{\mathrm{N}} = 0.001$) of the nonlinear region. The pressure perturbation is plotted on the left in Figure 16 at three different time instants as the shock moves past a single cell centred at $x = 0.0105$. Close-up views of the pressure perturbation in the nonlinear region are shown in the insets on the left while the pressure itself is plotted separately on the right to show the shock motion. Though the incoming wave has a smooth Gaussian profile, the insets show that spurious oscillations are generated in a regular fashion on the subsonic (right) side of the shock as the it traverses the cell. The spikes were observed to occur when the shock crosses from one cell to another. The

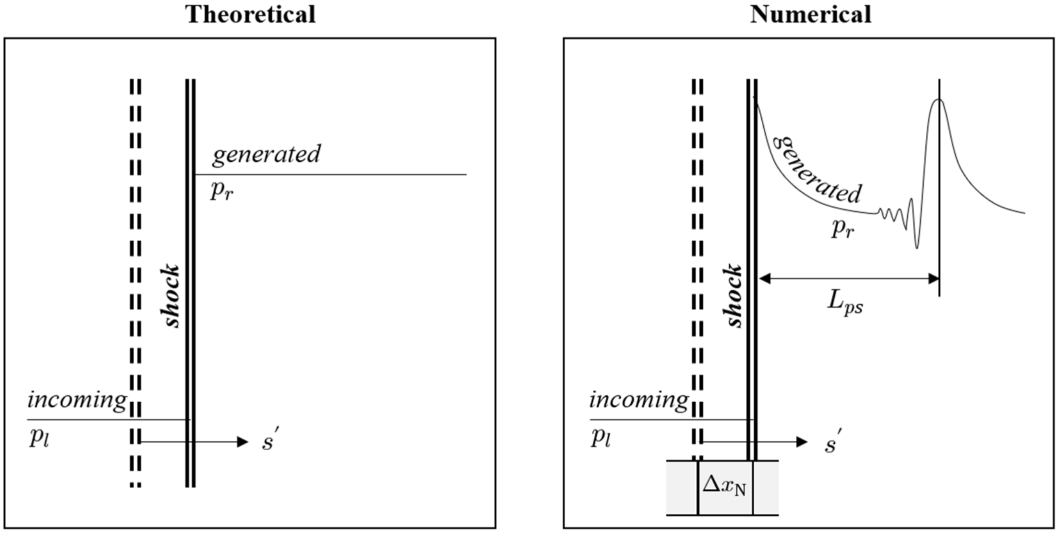

Figure 17: Comparison of theoretical and numerical behaviour for slow-moving shocks. Thick dashed lines and thick solid lines denote the initial and final shock positions, respectively.

amplitude of the generated perturbation depends on the position of the shock within the cell as shown in Figure 16.

The spurious post-shock oscillations observed in Figure 16 arise due to the well-known drawback that upwind numerical flux schemes experience when computing slow-moving shocks [40]. A shock is said to be slow-moving if $s'/s_{max} \ll 1$ where s' is the shock speed and s_{max} is the maximum wave speed given by $s_{max} = \max(|u_l| + c_l, |u_r| + c_r)$ [41]. Let us consider the passage of a slow-moving shock across a single cell of width Δx_{N} (refer to schematic in Figure 17), which will generate one cycle of post-shock oscillations. In this consideration, the shock is initially positioned at the cell interface and the incoming perturbation has a constant amplitude ϵ. From LIA (see Appendix A1), the shock speed $s'{\sim}\mathrm{O}(\epsilon)$ is constant and the resulting perturbations are also constant. However, the generated perturbations have nonuniform profiles because of the post-shock oscillations from the slow-moving shock. It has been established earlier that the generated perturbation has an acoustic component travelling at a speed of $u_r + c_r$ and an entropic component travelling at a slower speed of u_r. Taking the faster propagation speed $u_r + c_r$, the generated perturbations would have travelled a distance of $L_{ps} \approx (u_r + c_r)\,\Delta x_{\mathrm{N}}/|s'|$ from the shock during the time it takes the shock to cross one cell. The length L_{ps} can be interpreted as the wavelength of one cycle of post-shock oscillations. For a slow-

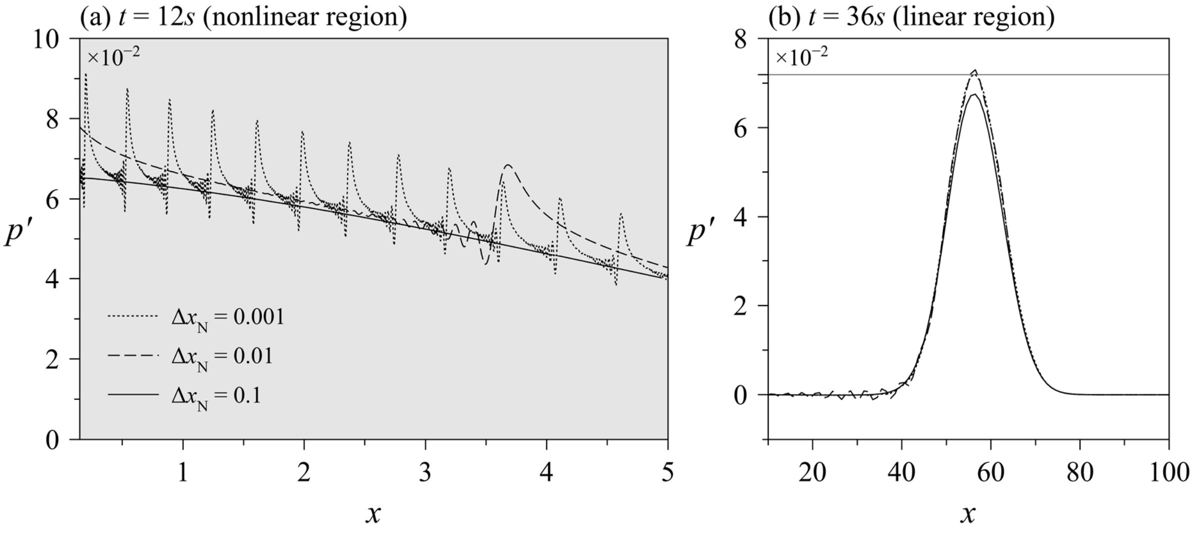

Figure 18: Pressure perturbations generated for the case of a $M = 3$ shock interacting with a $u_l + c_l$ wave of amplitude $\epsilon = 10^{-2}$ for three different nonlinear region mesh resolutions.

moving shock with $(u_r + c_r)/s' \gg 1$, L_{ps} is several times larger than the cell width Δx_{N}. Assuming that the shock is perfectly positioned at the next cell interface after crossing one cell, conservation dictates that the average perturbation amplitude over the wavelength L_{ps} be equal to the uniform value derived from LIA. In the domain decomposition technique, the nonlinear region is discretized using a much finer mesh compared to the linear region, i.e., $\Delta x_{\mathrm{N}} < \Delta x_{\mathrm{L}}$. If the linear region cell spacing Δx_{L} is larger than the wavelength L_{ps}, the volumetric mapping from the nonlinear region to the linear region is tantamount to an averaging process. Therefore, the mapping process eliminates the post-shock oscillations and recovers the correct theoretical amplitude for the generated wave.

When the nonlinear region mesh is refined ($\Delta x_{\mathrm{N}} \downarrow$), the wavelength of one cycle of post-shock oscillations L_{ps} becomes shorter, and vice versa. Figure 18 shows the results obtained at three different mesh resolutions (uniform spacing of $\Delta x_{\mathrm{N}} = 0.001, 0.01$ and 0.1) for the nonlinear region for the case of a $M = 3$ shock interacting with a $u_l + c_l$ wave of amplitude $\epsilon = 10^{-2}$. The linear region mesh resolution was kept at $\Delta x_{\mathrm{L}} = 1$ for all three cases. The pressure perturbations within the nonlinear region at $t = 12s$ are plotted in Figure 18(a) to illustrate the post-shock oscillations generated as the incoming $u_l + c_l$ wave is interacting with the shock. It can be seen from Figure 18(a) that the wavelength L_{ps} increases as the nonlinear region mesh is coarsened. At the coarsest resolution $\Delta x_{\mathrm{N}} =$

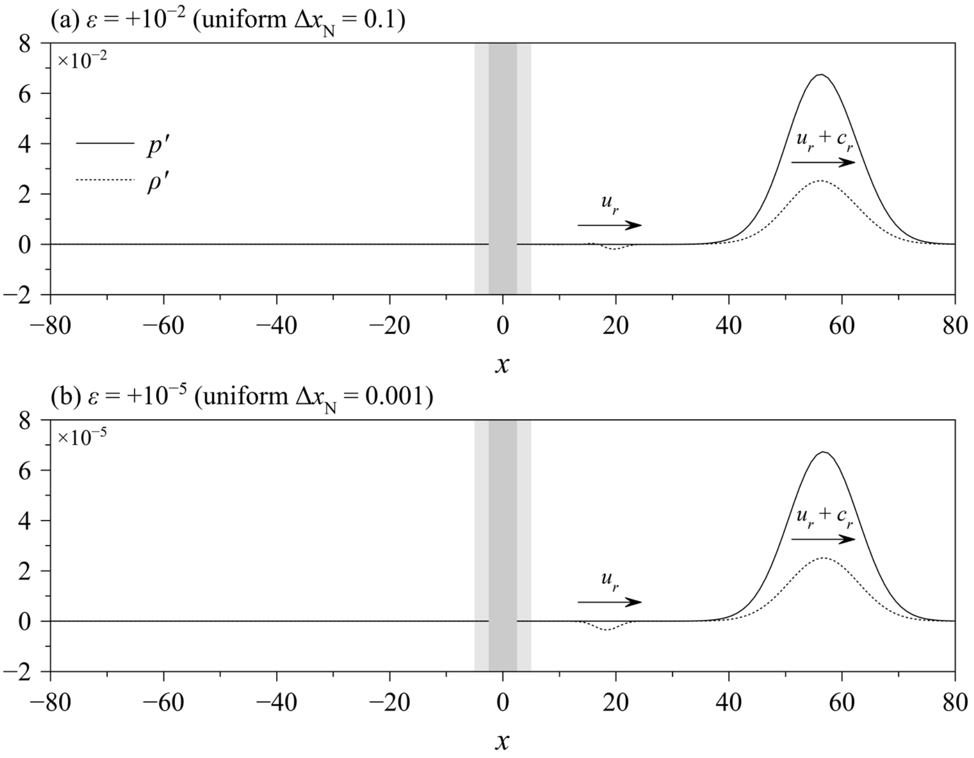

Figure 19: Interaction of a $u_l + c_l$ acoustic wave with a $M = 3$ standing shock at $t = 36s$.

0.1, the shock does not fully cross even one cell and, thus, only a partial cycle of post-shock oscillations is generated. The pressure perturbations within the linear region at a later time $t = 36s$ are plotted in Figure 18(b) to show the $u_r + c_r$ wave generated. The horizontal grey line indicates the theoretical peak amplitude. The peak amplitude of the $u_r + c_r$ wave deviates from the theoretical prediction by -6.07%, $+1.54\%$ and $+0.064\%$ at the mesh resolutions $\Delta x_{\mathrm{N}} = 0.1$, 0.01 and 0.001, respectively. Though the peak amplitude is captured relatively well at the intermediate resolution $\Delta x_{\mathrm{N}} = 0.01$, the solution is contaminated by small spurious oscillations that do not appear at the finest resolution $\Delta x_{\mathrm{N}} = 0.001$.

These results suggest that, to obtain accurate results, the interaction of the shock with the incoming perturbation should displace the shock by a few cell widths so that several cycles of post-shock oscillations can be generated and averaged. This explains the deviations from theoretical predictions observed earlier in Figure 15. The shocks were displaced by several cell widths for the $|\epsilon| = 10^{-2}$ cases computed using $\Delta x_{\mathrm{N}} = 0.001$, generating many cycles of post-shock oscillations. In contrast, the shocks were displaced by only a fraction of a cell width for the $|\epsilon| = 10^{-5}$ cases computed using $\Delta x_{\mathrm{N}} = 0.001$, similar to the $|\epsilon| = 10^{-2}$ cases computed using $\Delta x_{\mathrm{N}} = 0.1$. A comparison between these two cases for $M = 3$ is shown in Figure 19. It can be seen that $\max(p'/\epsilon) \approx 6.7$ in both cases as opposed to the expected value of 7.1 predicted by LIA. This proves that insufficient mesh resolution led to the large discrepancies in the amplification factors for $|\epsilon| = 10^{-5}$ cases.

3.4 Areas to Explore in Future Work

The domain decomposition technique presented in this paper has been developed with the aim of simulating realistic thermo-acoustic problems in higher dimensions. There still remain several areas for improving the technique that are being actively pursued. In this section, preliminary results from two such areas of investigation are presented.

3.4.1 Heat Addition

It is imperative that the domain decomposition technique is able to handle the effects of heat addition properly for simulating thermo-acoustic problems. In many of the problems, heat addition is often restricted to small, localized regions. These problems can be best solved using the domain decomposition technique as the nonlinear solver can be used in the localized heat addition region and the linearized solver can be used for the propagation of the small disturbances.

One such problem is the interaction of an acoustic wave with heated supersonic flow where heat is added (Rayleigh heating) over a localized region resulting in continuous but steep flow gradients. This problem is similar in configuration to the shock-acoustic/entropy wave interaction problems studied in the earlier section. The problem was solved in two steps. First, the one-dimensional flow problem with heat addition was solved using the nonlinear solver to obtain a steady-state solution. Then, the interaction of the acoustic wave with the heated flow was solved using the domain decomposition technique with the nonlinear region initialized with the steady-state solution obtained earlier.

For the heated flow problem, a specific heat addition rate $\dot{q}$ was included on the right-hand-side of the total energy equation as a source term as follows:

$$\partial_t(\rho e_t) + \partial_x(\rho e_t u + pu) = \dot{q}. \tag{29}$$

The domain for the nonlinear computation $x \in [-10,10]$ was discretized uniformly into cells of width $\Delta x_N = 0.1$. The left and right Mach numbers were chosen as $M_l = 3$ and $M_r = 2$, respectively. The left and right states given below were determined based on mass and momentum conservation:

$$\mathbf{U}_l = (\rho, u, p)_l = (1.4, 3, 1), \qquad \mathbf{U}_r = (\rho, u, p)_r = (1.528676, 2.747475, 2.060606). \tag{30}$$

The heat source was prescribed as follows within the nonlinear region to effect the proper change in total temperature from the left state to the right.

$$\dot{q} = 1.766297 \cdot G\left(x; 0, \tfrac{5}{3}\right) \tag{31}$$

The heat source is concentrated in the zone $x \in [-5,5]$ to produce steep flow gradients. The problem was initialized with the primitive variables smoothly transitioning from $\mathbf{U}_l$ to $\mathbf{U}_r$ over the region of heat source. Subsequently, $\mathbf{U}_l$ was specified at the left boundary while a Neumann boundary condition was applied at the right boundary. The computation was performed using a time step of $\Delta t = 0.01s$ until the density residual dropped below 10^{-12}.

For the acoustic wave interaction problem, the linear region extends between $x \in [-150,350]$ and terminates in sponge layers of lengths $L_x = 50$. It was uniformly discretized using cells of width $\Delta x_L = 1$. The mean state in the linear region was initialized as,

$$\overline{\mathbf{U}}(x, 0) = \begin{cases} \mathbf{U}_l, & x < 0 \\ \mathbf{U}_r, & x > 0 \end{cases}, \tag{32}$$

and a $u_l + c_l$ acoustic wave was initialized as,

$$\begin{aligned} p'(x, 0) &= \epsilon \mathrm{G}(x; -50,12), \\ u'(x, 0) &= \tfrac{\epsilon}{1.4} \mathrm{G}(x; -50,12), \\ \rho'(x, 0) &= \epsilon \mathrm{G}(x; -50,12), \end{aligned} \tag{33}$$

with $\epsilon = 10^{-2}$. The nonlinear region, which is identical to the domain used for the nonlinear computation, was initialized with the steady-state solution. The problem was computed using a time step of $\Delta t = 0.01s$ until $t = 100s$.

p' and ρ' profiles at five different instants are plotted in Figure 20. The Mach number profile in the nonlinear region at $t = 0s$ is included in Figure 20(a). As the localized heat is added to the flow continuously in a steady manner, the Mach number does not change significantly as the disturbances propagate through the heated flow. In the interaction with shock wave cases discussed earlier, the flow in the nonlinear region is altered permanently due to the shock motion. However, for the case of heat addition, the flow in the nonlinear region returns to its initial state since the heat addition does not vary in time. As the flow remains continuous and no shock waves are formed, there are no post-shock oscillations as observed previously. The $u_l + c_l$ acoustic wave interacts with the heated flow to produce a $u_r - c_r$ wave, a u_r wave and a $u_r + c_r$ wave. All waves propagate towards the right as the flow is supersonic everywhere. A linearized analysis was performed for this problem to determine the amplification ratios of ρ' for the three waves (see Appendix A2 for analysis). The amplification ratios obtained from the computed results are compared with the theoretical predictions in Table 3, showing that the numerical results agree well with the theoretical predictions.

3.4.2 Imperfect Overlap

In the test cases mentioned thus far, the domain was decomposed such that the overset boundary on either side coincided with a linear region cell interface. However, to achieve coincidence of overset boundaries with the linear region cell interfaces in higher dimensions, additional efforts during grid generation may be required. Hence, the effect of imperfect overlap of the overset boundary and the linear region is worth investigating.

For this investigation, the propagation of an acoustic wave test case described in the Section 3.2.1 was first computed using a cell size ratio of $R = 4$ until $t = 65s$ when the acoustic wave has moved into the nonlinear region completely. Then, the computation was repeated with one, two, and three leftmost nonlinear region cells removed so that the left overset boundary shifts to the right by Δx_{N}, $2\Delta x_{\mathrm{N}}$, and $3\Delta x_{\mathrm{N}}$, respectively. Close-up views near the left overset boundary for the four cases are shown in Figure 21. Upon the fourth removal, the left overset boundary coincides with a linear region cell interface again; so, only three removals need to be considered. Each case is designated by an overlap

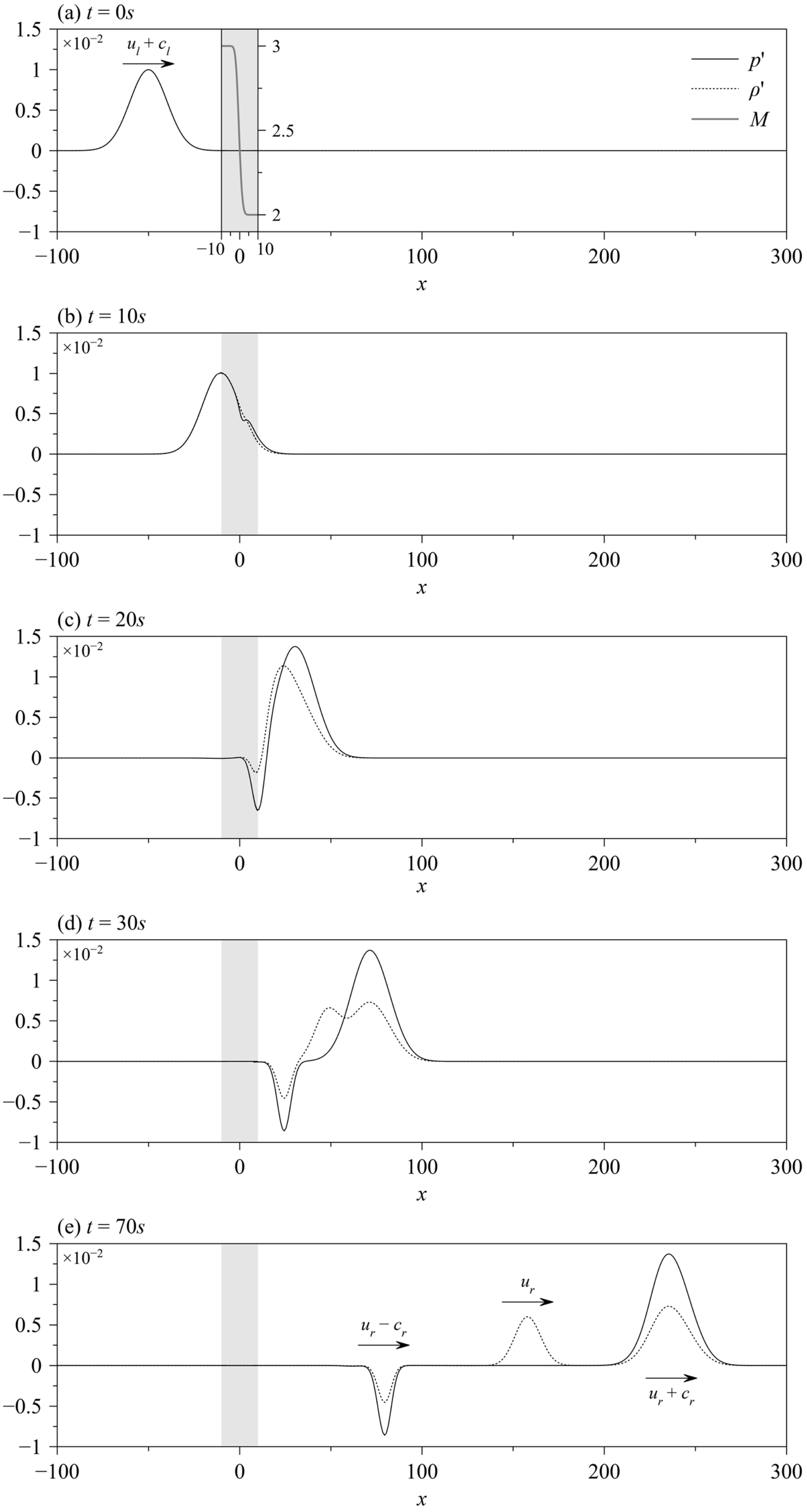

Figure 20: Interaction of a $u_l + c_l$ acoustic wave with heated supersonic flow.

Table 3: Amplification ratios of ρ' for the interaction of a $u_l + c_l$ acoustic wave with heated supersonic flow.

Wave type	Computed	Theoretical	Error
$u_r - c_r$	-0.4552	-0.4682	$+2.78\%$
u_r	0.5995	0.5966	$+0.49\%$
$u_r + c_r$	0.7293	0.7289	$+0.05\%$

percentage S, which is 100% for the case of perfect coincidence and reduces by 25% for each subsequent case. There are two points that are worth mentioning here. First, as soon as the first nonlinear region cell is removed, the leftmost mapped cell in the linear region is no longer completely overlapped by the nonlinear region and must be computed. To compensate for the 'loss' of a mapped cell, the leftmost hole cell is set to be mapped. Second, the linear region cell that was selected for interpolation at the overset boundary for the first three cases ($S \geq 50\%$) is different from that selected for the last case ($S = 25\%$). This is because, upon the removal of the third nonlinear region cell, the left overset boundary shifts past the centroid of a new linear region cell, which is closer to the boundary compared to the previously selected cell. Hence, this new cell is selected for interpolation.

In Figure 22, $\rho'(x, t)$ are plotted at $t = 65s$ when the acoustic wave has just passed through the left overset boundary into the nonlinear region. For $S = 100\%$ and 25%, the computed profiles are nearly identical to the exact solution. As for $S = 50\%$ and 75%, a slight drop in the peak amplitude and a small phase shift can be observed. Odd-even oscillations are generated in all cases as the acoustic wave moves past the left overset boundary. These oscillations travel in the opposite direction to the acoustic wave. They are responsible for the periodic bumps observed in the error profiles in Figure 11 contributing to the coupling error discussed in the Section 3.2.1. For $S = 100\%$ and 25%, the spurious oscillations have an amplitude of $\sim 10^{-3}\epsilon$, i.e., about three orders of magnitude smaller than the amplitude of the physical density perturbation. However, it increases by an order of magnitude to $\sim 10^{-2}\epsilon$ for $S = 50\%$ and 75%.

Comparing Figures 21 and 22, it can be observed that the closer the overset boundary face lies to the centroid of the linear region cell involved in the interpolation, the smaller the amplitude of the spurious

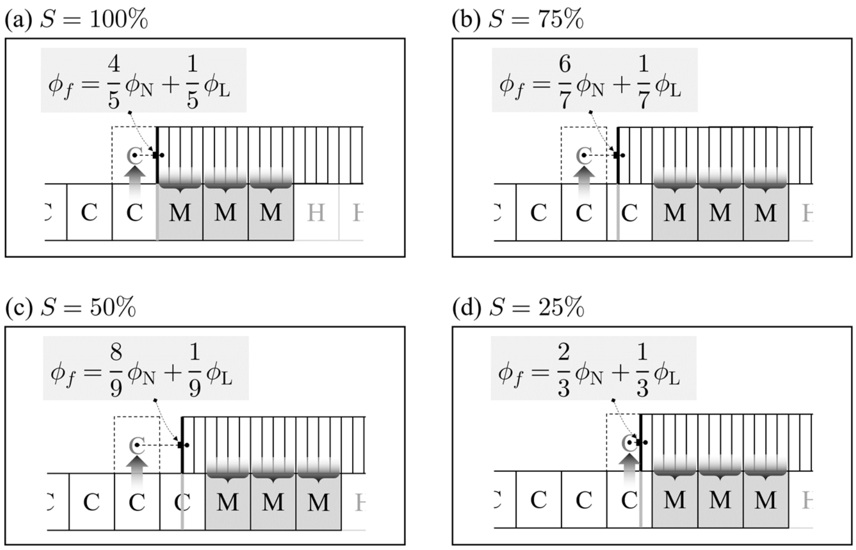
(a) $S = 100\%$
(b) $S = 75\%$
(c) $S = 50\%$
(d) $S = 25\%$

Figure 21: Linear interpolation coefficients at left overset boundary for different overlap percentages.

oscillations. In one dimension, expanding the linear interpolation at the overset boundary face (see Eq. (15)) using Taylor series about the face centroid x_f yields the following:

$$\mathbf{U}_f = \mathbf{U}(x_f) + \frac{d^2\mathbf{U}}{dx^2}(x_f)\left[\frac{|x_\mathrm{L} - x_f|\Delta x_\mathrm{N}}{4} + \frac{\Delta x_\mathrm{N}^2}{24}\right] + \mathrm{H.O.T.} \quad . \tag{34}$$

For a fixed Δx_N, the leading order error term increases with $|x_\mathrm{L} - x_f|$, which is the distance from the overset boundary face centroid to the centroid of the linear region cell involved in the interpolation. This indicates that the interpolation accuracy at the overset boundary might play an important role in the generation of the oscillations. Past studies [42, 43] have concluded that coupling linear interpolation scheme with the DRP interpolation scheme results in large interpolation errors and that these errors can be minimized by the use of high-order interpolation. However, high-order interpolations are still prone to generating high-wavenumber spurious modes [44]. Filtering can be used to reduce the spurious oscillations more effectively. Thus, the four cases were recomputed with high-order interpolation and filtering. Interpolation at each overset boundary face was performed using a fourth order Lagrange interpolation to match the formal order of accuracy of the DRP interpolation scheme used in the linear region. The interpolation involved four linear region cells, two calculated (C) and two mapped (M), near the overset boundary. A 9-point optimized selective filter [45] was applied to the perturbed

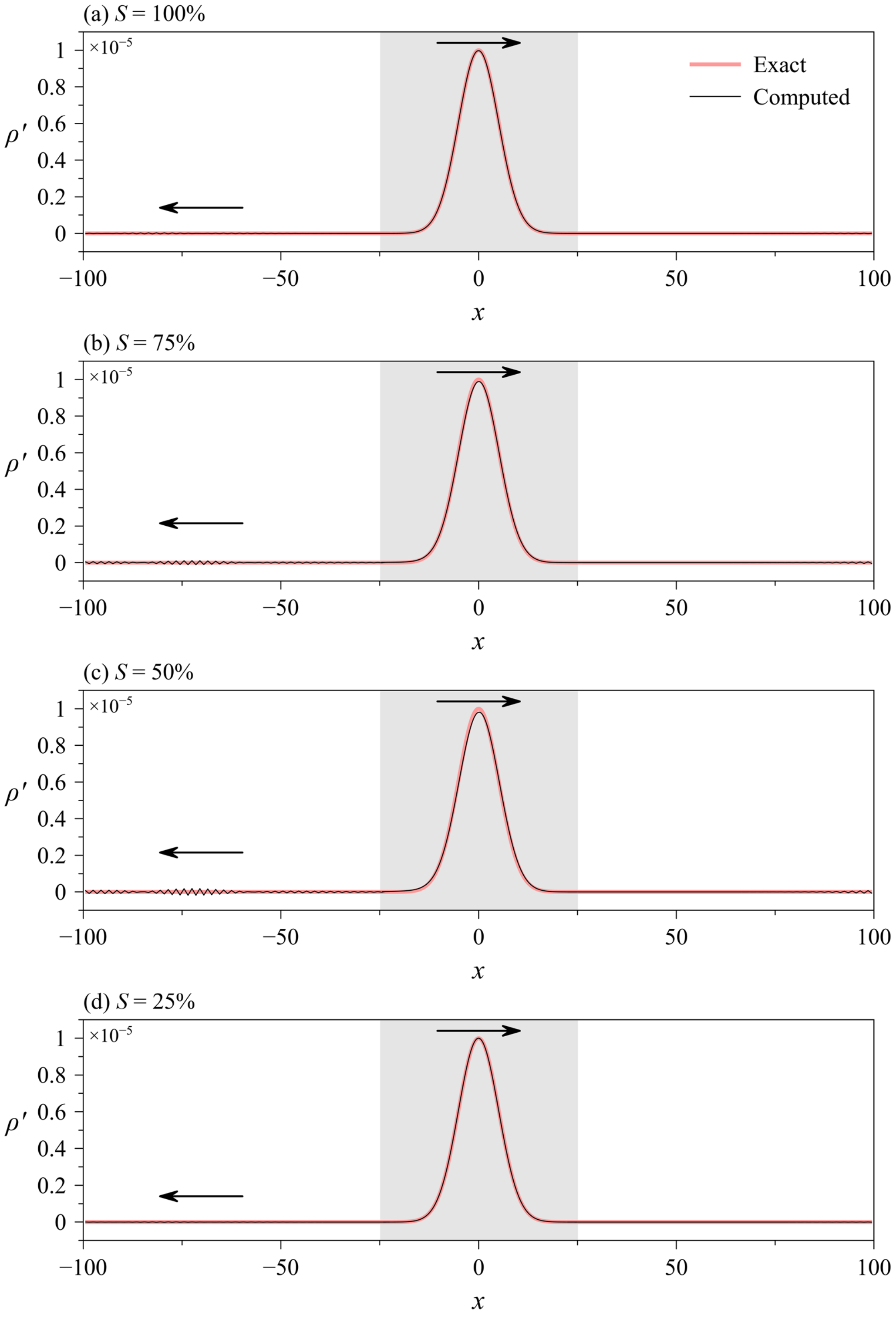
(a) $S = 100\%$

(b) $S = 75\%$

(c) $S = 50\%$

(d) $S = 25\%$

Figure 22: Results for propagation of single acoustic wave for different overlap percentages at $t = 65s$.

conserved variables $\mathbf{Q}'$ at the last Runge-Kutta stage of each time step. The symmetric 9-point filter required four mapped (M) cells near each overset boundary. Two filter strengths $\sigma_d = 5 \times 10^{-3}$ and 5×10^{-2} were investigated.

Table 4: Average density perturbation errors $\widehat{\rho'}$ for the propagation of a single acoustic wave computed for different overlap percentages with different interpolation schemes and filter strengths.

Interpolation scheme	σ_d	$S = 100\%$	$S = 75\%$	$S = 50\%$	$S = 25\%$
Linear	0	$5.9162e{-9}$	$2.7899e{-8}$	$4.7577e{-8}$	$3.1399e{-9}$
	5×10^{-3}	$3.8091e{-9}$	$1.8050e{-8}$	$3.1049e{-8}$	$2.3005e{-9}$
	5×10^{-2}	$2.7477e{-9}$	$9.8832e{-9}$	$1.7063e{-8}$	$1.8287e{-9}$
Fourth order Lagrange	0	$3.0681e{-9}$	$2.5754e{-9}$	$2.4192e{-9}$	$2.5811e{-9}$
	5×10^{-3}	$2.2507e{-9}$	$2.0472e{-9}$	$1.9882e{-9}$	$2.0362e{-9}$
	5×10^{-2}	$1.8087e{-9}$	$1.7163e{-9}$	$1.6908e{-9}$	$1.6889e{-9}$

The average density perturbation errors $\widehat{\rho'}$ at $t = 65s$ for the original and recomputed cases are listed in Table 4. The unfiltered cases are denoted by $\sigma_d = 0$. It can be seen that high-order interpolation results in an order of magnitude improvement in accuracy for $S = 50\%$ and 75% cases and also slight improvements for $S = 100\%$ and 25% cases. The improvement in accuracy due to filtering occurs primarily because of the attenuation of the odd-even oscillations. The odd-even oscillations were completely eliminated at $\sigma_d = 5 \times 10^{-2}$. For any value of S, the best result is obtained when using both high-order interpolation and filtering. Hence, high-order interpolation and filtering will be extended to the multi-dimensional implementation of the domain decomposition technique.

4 Conclusion

In this paper, a domain decomposition technique was presented in the finite volume framework whereby the computational domain is divided into two overlapping regions: a nonlinear region that can be discretized into a non-uniform or even unstructured mesh for maximum geometric flexibility and a linear region that is always discretized into a uniform Cartesian mesh for ease of implementing high-order spatial discretization schemes. In the nonlinear region, the nonlinear Euler equations are solved with the interfacial fluxes computed using a second order hybrid central/upwind flux scheme. In the linear region, the linearized Euler equations are solved with the linearized fluxes computed using a fourth order DRP scheme. The solutions in both regions are time marched in tandem using an explicit fourth order LDDRK scheme. Two-way coupling is established between the regions using volumetric mapping of conserved variables from the nonlinear region onto the linear region and interpolation of the mean and perturbed primitive variables at the boundary faces of the nonlinear region.

The domain decomposition technique was applied to investigate the interaction of incident acoustic and entropy waves with a normal shock wave. The key conclusions drawn from the numerical results are as follow:

- Comparing the nonlinear solver to the linear solver for propagation of acoustic waves, it is observed that the nonlinear solver requires ten times the mesh resolution and forty times the computational time to achieve comparable accuracy as the linear solver. This is caused by the excessive dispersion errors associated with the nonlinear solver, and low dispersion and dissipation characteristics of the linear solver.
- Domain decomposition procedure was successfully implemented to propagate acoustic and entropy waves from a linear region to a nonlinear region and vice versa. Spurious odd-even oscillations are generated as a wave crosses the overset boundaries, but they are several orders of magnitude smaller than the amplitude of the propagating wave itself. These oscillations can be effectively eliminated by using high-order interpolation at the overset boundary and filtering. The domain decomposition solver was successful in reducing the computational time of the nonlinear solver by a factor of three while maintaining the same accuracy of the dense mesh needed for the nonlinear solver.
- It is necessary to use smaller cells in the nonlinear region to minimize the dispersion error arising from the use of second order schemes. Even at modest cell size ratios, the domain decomposition technique produces more accurate results compared to the linear solver.
- The domain decomposition technique proved to be effective in solving the shock-acoustic/entropy wave interaction problem. It was observed that the amplitude of the waves generated depended on the shock position within the cell. Agreement with linear theory was obtained in cases whereby the shock was displaced by several cell widths producing several

cycles of post-shock oscillations. The nonlinear-to-linear mapping process helped to average the post-shock oscillations and capture the correct amplitudes for the generated waves.

Further studies will be conducted to explore the application of the domain decomposition technique for problems in higher dimensions. Independent time-marching using different time steps in the two regions will also be considered as we apply the schemes for time varying mean flows.

Appendix

A1 Linearized Interaction Analysis (LIA) for Interaction of an Acoustic/Entropy Wave with Normal Shock

Equations (A1), (A2) and (A3) collectively represent the Rankine-Hugoniot (RH) relationships connecting the left and right states of a steady normal shock for a calorically perfect ideal gas.

$$\rho_l u_l = \rho_r u_r \tag{A1}$$

$$\frac{\gamma R T_l}{\gamma - 1} + \frac{1}{2} u_l^2 = \frac{\gamma R T_r}{\gamma - 1} + \frac{1}{2} u_r^2 \equiv h_t \tag{A2}$$

$$u_l u_r = 2 \frac{\gamma - 1}{\gamma + 1} h_t \tag{A3}$$

From the ideal gas relation, it can be shown that,

$$T' = \bar{T} \left(\frac{p'}{p} - \frac{\rho'}{\rho} \right). \tag{A4}$$

Suppose that a perturbation $(p_l', \rho_l', T_l', u_l')$ is introduced to the supersonic (left) state. This generates a corresponding perturbation $(p_r', \rho_r', T_r', u_r')$ to the subsonic (right) state and causes the shock to move at a speed of s'. Applying the RH relationships in the frame moving at the shock speed s' yields the following relationships. Note that the total enthalpy h_t in Eq. (A7) has been written in terms of the left state since the perturbation to the left state is known.

$$(\overline{\rho_l} + \rho_l')(\overline{u_l} + u_l' - s') = (\overline{\rho_r} - \rho_r')(\overline{u_r} + u_r' - s') \tag{A5}$$

$$\frac{\gamma R(\overline{T_l} + T_l')}{\gamma - 1} + \frac{1}{2}(\overline{u_l} + u_l' - s')^2 = \frac{\gamma R(\overline{T_r} + T_r')}{\gamma - 1} + \frac{1}{2}(\overline{u_r} + u_r' - s')^2 \tag{A6}$$

$$(\overline{u_l} + u_l' - s')(\overline{u_r} + u_r' - s') = 2 \frac{\gamma - 1}{\gamma + 1} \left[\frac{\gamma R(\overline{T_l} + T_l')}{\gamma - 1} + \frac{1}{2}(\overline{u_l} + u_l' - s')^2 \right] \tag{A7}$$

Subtracting Eqs. (A1), (A2) and (A3) from Eqs. (A5), (A6) and (A7), respectively, and the result from Eq. (A4) yields the perturbed RH relationships.

$$\overline{\rho_l}(u_l' - s') + \rho_l' \overline{u_l} = \overline{\rho_r}(u_r' - s') + \rho_r' \overline{u_r} \tag{A8}$$

$$\frac{\gamma R \overline{T_l}}{\gamma - 1} \left(\frac{p_l'}{\overline{p_l}} - \frac{\rho_l'}{\overline{\rho_l}} \right) + \overline{u_l}(u_l' - s') = \frac{\gamma R \overline{T_r}}{\gamma - 1} \left(\frac{p_r'}{\overline{p_r}} - \frac{\rho_r'}{\overline{\rho_r}} \right) + \overline{u_r}(u_r' - s') \tag{A9}$$

$$\overline{u_l}(u_r' - s') + \overline{u_r}(u_l' - s') = \frac{2\gamma R\overline{T_l}}{\gamma + 1}\left(\frac{p_l'}{\overline{p_l}} - \frac{\rho_l'}{\overline{\rho_l}}\right) + \frac{2(\gamma - 1)}{\gamma + 1}\overline{u_l}(u_l' - s') \tag{A10}$$

Since the interaction with the shock always produces a u_r entropy wave and a $u_r + c_r$ acoustic wave on the subsonic side, the perturbations to the right state can be expressed in terms of p_r' as follows. Note that the density perturbation ρ_r' consists of two components – the first component is related to the $u_r + c_r$ wave while the second component ρ_{ru}' is related to the u_r wave.

$$\rho_r' = \frac{p_r'}{\overline{c_r^2}} + \rho_{ru}', \qquad u_r' = \frac{p_r'}{\overline{\rho_r c_r}} \tag{A11}$$

The perturbation introduced to the left state can be acoustic or entropic. To generalize the derivation for a $u_l + \alpha c_l$ wave where $\alpha \in [-1,0,1]$, the pressure and velocity perturbations are expressed in terms of the density perturbation ρ_l' as follows.

$$p_l' = |\alpha|\rho_l'\overline{c_l^2}, \qquad u_l' = \alpha\frac{\rho_l'\overline{c_l}}{\overline{\rho_l}} \tag{A12}$$

Substituting Eqs. (A11) and (A12) into Eqs. (A8)-(A10) and simplifying yields the following system of linear equations where $M_r \equiv \overline{u_r}/\overline{c_r}$.

$$\begin{bmatrix} M_r + 1 & \overline{u_r c_r} & (\overline{\rho_l} - \overline{\rho_r})\overline{c_r} \\ (\gamma - 1)(M_r + 1) & -\overline{c_r^2} & (\gamma - 1)\overline{\rho_r}(\overline{u_l} - \overline{u_r}) \\ M_r & 0 & \overline{\rho_l}\left(\frac{\gamma - 3}{\gamma + 1}\overline{u_l} - \overline{u_r}\right) \end{bmatrix} \begin{pmatrix} p_r' \\ \rho_{ru}' \\ s' \end{pmatrix} = \begin{pmatrix} (\overline{u_l} + \alpha\overline{c_l})\overline{c_r} \\ \frac{\overline{\rho_r}}{\overline{\rho_l}}\left[(|\alpha|\gamma - 1)\overline{c_l^2} + \alpha(\gamma - 1)\overline{u_l c_l}\right] \\ \frac{2(|\alpha|\gamma - 1)\overline{c_l^2} + \alpha[2(\gamma - 1)\overline{u_l} - (\gamma + 1)\overline{u_r}]\overline{c_l}}{(\gamma + 1)} \end{pmatrix}\rho_l' \tag{A13}$$

The above system of linear equations can be solved numerically to determine the amplitudes p_r' and ρ_{ru}', and the shock speed s'.

A2 Linearized Analysis for Interaction of an Acoustic Wave with Heated Supersonic Flow

A schematic of the flow problem is shown in Figure A1. Heat addition causes the flow to change from the left state to the right state which are denoted by the subscripts 'l' and 'r', respectively. The Mach number reduces due to heat addition but still remains supersonic, i.e. $M_l > M_r > 1$. Interaction of the incoming $u_l + c_l$ wave with the heated flow generates a $u_r - c_r$ wave in addition to a u_r wave and a $u_r + c_r$ wave. The incoming $u_l + c_l$ wave has a wavelength of λ_1 and an amplitude of $\rho' = \epsilon$. The wavelengths of the $u_r - c_r$, u_r and $u_r + c_r$ waves are denoted by λ_2, λ_3 and λ_4, respectively. ρ' amplitudes for the three waves are expressed in terms of ϵ.

Unlike in the case of shock interaction, the mean flow remains steady throughout the interaction. Therefore, the perturbations of conserved variables $\mathbf{Q}'$ are *also* conserved in the interaction. Equating the integral of $\mathbf{Q}'$ over the interval $(-\infty, \infty)$ at two different times t_1 and t_2, and ignoring higher order product terms yields the following.

$$\int_{-\infty}^{+\infty} \rho'(x,t_2)\ dx = \int_{-\infty}^{+\infty} \rho'(x,t_1)\ dx \tag{A14}$$

$$\begin{aligned}&\int_{-\infty}^{+\infty} \rho'(x,t_2)\bar{u}(x,t_2) + \bar{\rho}(x,t_2)u'(x,t_2)\ dx\\ &= \int_{-\infty}^{+\infty} \rho'(x,t_1)\bar{u}(x,t_1) + \bar{\rho}(x,t_1)u'(x,t_1)\ dx\end{aligned} \tag{A15}$$

$$\begin{aligned}&\int_{-\infty}^{+\infty} \frac{p'(x,t_2)}{\gamma-1} + \frac{1}{2}\rho'(x,t_2)\bar{u}^2(x,t_2) + \bar{\rho}(x,t_2)\bar{u}(x,t_2)u'(x,t_2)\ dx\\ &= \int_{-\infty}^{+\infty} \frac{p'(x,t_1)}{\gamma-1} + \frac{1}{2}\rho'(x,t_1)\bar{u}^2(x,t_1) + \bar{\rho}(x,t_1)\bar{u}(x,t_1)u'(x,t_1)\ dx\end{aligned} \tag{A16}$$

Though the above relationships hold for any two instants t_1 and t_2, the analysis can be considerably simplified by choosing t_1 to be well before the incoming wave interacts with the heated flow and t_2 to be well after the three generated waves have propagated away from the heated flow and separated into individual waves due to the difference in propagation speeds. This is illustrated in Figure A1. Assuming that all the waves have a top-hat profile, substituting the relationships,

(a) Before interaction

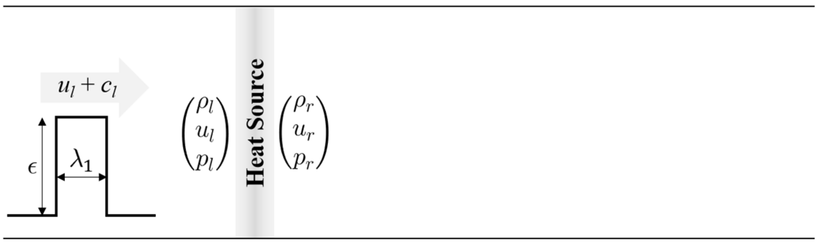

(b) After interaction

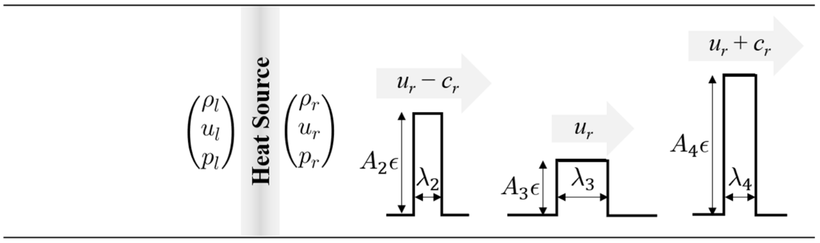

Figure A1: Schematic of acoustic wave interaction with heated supersonic flow. Waves are illustrated in terms of density perturbations ρ'.

$$
\begin{aligned}
u_l + c_l \text{ wave: } \begin{pmatrix}\rho'\\ u'\\ p'\end{pmatrix} &= \epsilon \begin{pmatrix}1\\ \overline{c_l}/\overline{\rho_l}\\ \overline{c_l^2}\end{pmatrix}, \\
u_r - c_r \text{ wave: } \begin{pmatrix}\rho'\\ u'\\ p'\end{pmatrix} &= A_2\epsilon \begin{pmatrix}1\\ -\overline{c_r}/\overline{\rho_r}\\ \overline{c_r^2}\end{pmatrix}, \\
u_r \text{ wave: } \begin{pmatrix}\rho'\\ u'\\ p'\end{pmatrix} &= A_3\epsilon \begin{pmatrix}1\\ 0\\ 0\end{pmatrix}, \\
u_r + c_r \text{ wave: } \begin{pmatrix}\rho'\\ u'\\ p'\end{pmatrix} &= A_4\epsilon \begin{pmatrix}1\\ \overline{c_r}/\overline{\rho_r}\\ \overline{c_r^2}\end{pmatrix}
\end{aligned}
\tag{A17}
$$

into Eqs. (A14)-(A16) results in the following.

$$
A_2\epsilon\lambda_2 + A_3\epsilon\lambda_3 + A_4\epsilon\lambda_4 = \epsilon\lambda_1 \tag{A18}
$$

$$
\begin{aligned}
&\left[A_2\epsilon\overline{u_r} + \overline{\rho_r}\left(-\frac{A_2\epsilon\overline{c_r}}{\overline{\rho_r}}\right)\right]\lambda_2 + A_3\epsilon\overline{u_r}\lambda_3 + \left[A_4\epsilon\overline{u_r} + \overline{\rho_r}\left(\frac{A_4\epsilon\overline{c_r}}{\overline{\rho_r}}\right)\right]\lambda_4 \\
&\qquad = \left[\epsilon\overline{u_l} + \overline{\rho_l}\left(\frac{\epsilon\overline{c_l}}{\overline{\rho_l}}\right)\right]\lambda_1
\end{aligned}
\tag{A19}
$$

$$
\begin{aligned}
&\left[\frac{A_2\epsilon\overline{c_r^2}}{\gamma-1} + \frac{1}{2}A_2\epsilon\overline{u_r^2} + \overline{\rho_r u_r}\left(-\frac{A_2\epsilon\overline{c_r}}{\overline{\rho_r}}\right)\right]\lambda_2 + \frac{1}{2}A_3\epsilon\overline{u_r^2}\lambda_3 \\
&+ \left[\frac{A_4\epsilon\overline{c_r^2}}{\gamma-1} + \frac{1}{2}A_4\epsilon\overline{u_r^2} + \overline{\rho_r u_r}\left(\frac{A_4\epsilon\overline{c_r}}{\overline{\rho_r}}\right)\right]\lambda_4 = \left[\frac{\epsilon\overline{c_l^2}}{\gamma-1} + \frac{1}{2}\epsilon\overline{u_l^2} + \overline{\rho_l}u_l\left(\frac{\epsilon\overline{c_l}}{\overline{\rho_l}}\right)\right]\lambda_1
\end{aligned}
\tag{A20}
$$

Note that the assumption of top-hat profile does not limit the validity of the analysis as any profile can be partitioned into a superposition of an infinite number of top-hats with infinitesimally small wavelengths. Simplifying Eqs. (A18)-(A20) and casting them into a linear system yields the following.

$$\begin{bmatrix} \dfrac{1}{\overline{u_r}-\overline{c_r}} & \dfrac{1}{\overline{u_r}} & \dfrac{1}{\overline{u_r}+\overline{c_r}} \\ \dfrac{\overline{c_r^2}}{\gamma-1}+\dfrac{1}{2}\overline{u_r^2}-\overline{u_r c_r} & \dfrac{1}{2}\overline{u_r^2} & \dfrac{\overline{c_r^2}}{\gamma-1}+\dfrac{1}{2}\overline{u_r^2}+\overline{u_r c_r} \end{bmatrix} \begin{pmatrix} A_2\dfrac{\lambda_2}{\lambda_1} \\ A_3\dfrac{\lambda_3}{\lambda_1} \\ A_4\dfrac{\lambda_4}{\lambda_1} \end{pmatrix} = \begin{pmatrix} \dfrac{1}{\overline{u_l}+\overline{c_l}} \\ \dfrac{\overline{c_l^2}}{\gamma-1}+\dfrac{1}{2}\overline{u_l^2}+\overline{u_l c_l} \end{pmatrix} \tag{A21}$$

The above linear system can be solved numerically for the quantities $A_k\frac{\lambda_k}{\lambda_1}$. Finally, the amplification ratios A_k can be obtained by approximating the wavelength ratios $\frac{\lambda_k}{\lambda_1}$ based on the propagation speeds as given below.

$$\frac{\lambda_2}{\lambda_1}=\frac{\overline{u_r}-\overline{c_r}}{\overline{u_l}+\overline{c_l}}, \qquad \frac{\lambda_3}{\lambda_1}=\frac{\overline{u_r}}{\overline{u_l}+\overline{c_l}}, \qquad \frac{\lambda_4}{\lambda_1}=\frac{\overline{u_r}+\overline{c_r}}{\overline{u_l}+\overline{c_l}} \tag{A22}$$

Acknowledgements

This research was funded by Ministry of Education, Singapore under the MOE AcRF Tier-1 Grant RG183/18.

References

[1] C.K.W. Tam and H.K. Tanna. Shock associated noise of supersonic jets from convergent-divergent nozzles. *Journal of Sound and Vibration*. 81:337-358, 1982

[2] J.M. Delery. Shock wave/turbulent boundary layer interaction and its control. *Progress in Aerospace Sciences*. 22:209-280, 1985

[3] L.S.G. Kovasznay. Turbulence in supersonic flow. *Journal of the Aeronautical Sciences*. 20:657-674, 1953

[4] C.K.W. Tam. Computational aeroacoustics: An overview of computational challenges and applications. *International Journal of Computational Fluid Dynamics*. 18:547-567, 2004

[5] C.K.W. Tam and J.C. Webb. Dispersion-relation-preserving finite difference schemes for computational acoustics. *Journal of Computational Physics*. 107:262-281, 1993

[6] B. El Hadidi and A. Hemeda, Efficient domain decomposition technique for solution of high amplitude acoustic wave scattering in nonuniform flows, *17th AIAA/CEAS Aeroacoustics Conference (32nd AIAA Aeroacoustics Conference)*. 2011, American Institute of Aeronautics and Astronautics.

[7] H.S. Ribner. *Convection of a pattern of vorticity through a shock wave*. NACA Technical Note 2864. NACA, 1954

[8] H.S. Ribner. *Shock-turbulence interaction and the generation of noise*. NACA Technical Note 3255. NACA, 1954

[9] F.K. Moore. *Unsteady oblique interaction of a shock wave with a plane disturbance*. NACA Technical Note 2879. NACA, 1954

[10] A.A. Hemeda and B. Elhadidi. Domain decomposition technique for solution of acoustic wave scattering. *AIAA Journal*. 52:408-418, 2014

[11] J. Larsson and S.K. Lele. Direct numerical simulation of canonical shock/turbulence interaction. *Physics of Fluids*. 21:126101, 2009

[12] S. Jamme, J.B. Cazalbou, F. Torres, and P. Chassaing. Direct numerical simulation of the interaction between a shock wave and various types of isotropic turbulence. *Flow, Turbulence and Combustion*. 68:227-268, 2002

[13] K. Mahesh, S.K. Lele, and P. Moin. The influence of entropy fluctuations on the interaction of turbulence with a shock wave. *Journal of Fluid Mechanics*. 334:353-379, 1997

[14] S. Lee, S.K. Lele, and P. Moin. Interaction of isotropic turbulence with shock waves: effect of shock strength. *Journal of Fluid Mechanics*. 340:225-247, 1997

[15] R. Hannappel and R. Friedrich. Direct numerical simulation of a Mach 2 shock interacting with isotropic turbulence. *Applied Scientific Research*. 54:205-221, 1995

[16] S. Lee, S.K. Lele, and P. Moin. Direct numerical simulation of isotropic turbulence interacting with a weak shock wave. *Journal of Fluid Mechanics*. 251:533-562, 1993

[17] K. Mahesh, S. Lee, S.K. Lele, and P. Moin. The interaction of an isotropic field of acoustic waves with a shock wave. *Journal of Fluid Mechanics*. 300:383-407, 1995

[18] G. Cunha and S. Redonnet, Towards a robust and accurate CFD/CAA coupling procedure for hybrid methods in aeroacoustics - Part 1: On the optimization of CFD/CAA coupled calculations, *18th AIAA/CEAS Aeroacoustics Conference (33rd AIAA Aeroacoustics Conference)*. 2012, American Institute of Aeronautics and Astronautics.

[19] O. Labbé, C. Peyret, G. Rahier, and M. Huet. A CFD/CAA coupling method applied to jet noise prediction. *Computers & Fluids*. 86:1-13, 2013

[20] S. Redonnet and G. Cunha. An advanced hybrid method for the acoustic prediction. *Advances in Engineering Software*. 88:30-52, 2015

[21] A. Langenais, F. Vuillot, J. Troyes, and C. Bailly, Numerical investigation of the noise generated by a rocket engine at lift-off conditions using a two-way coupled CFD-CAA method, *23rd AIAA/CEAS Aeroacoustics Conference*. 2017, American Institute of Aeronautics and Astronautics.

[22] A. Langenais, F. Vuillot, C. Peyret, G. Chaineray, and C. Bailly. Assessment of a two-way coupling methodology between a flow and a high-order nonlinear acoustic unstructured solvers. *Flow, Turbulence and Combustion*. 101:681-703, 2018

[23] J.B. Freund. Proposed inflow/outflow boundary condition for direct computation of aerodynamic sound. *AIAA Journal*. 35:740-742, 1997

[24] F.Q. Hu. Development of PML absorbing boundary conditions for computational aeroacoustics: A progress review. *Computers & Fluids*. 37:336-348, 2008

[25] T.J. Poinsot and S.K. Lele. Boundary conditions for direct simulations of compressible viscous flows. *Journal of Computational Physics*. 101:104-129, 1992

[26] C. Bogey and C. Bailly. Three-dimensional non-reflective boundary conditions for acoustic simulations: far field formulation and validation test cases. *Acta Acustica united with Acustica*. 88:463-471, 2002

[27] A. Mani. Analysis and optimization of numerical sponge layers as a nonreflective boundary treatment. *Journal of Computational Physics*. 231:704-716, 2012

[28] A. Bhagatwala and S.K. Lele. A modified artificial viscosity approach for compressible turbulence simulations. *J. Comput. Phys.*, 228:4965-4969, 2009

[29] U S Vevek, B. Zang, and T.H. New. An efficient hybrid method for solving Euler equations. *J. Sci. Comput.*, 81:732-762, 2019

[30] E.F. Toro, M. Spruce, and W. Speares. Restoration of the contact surface in the HLL-Riemann solver. *Shock Waves*. 4:25-34, 1994

[31] P. Batten, N. Clarke, C. Lambert, and D. Causon. On the choice of wavespeeds for the HLLC Riemann solver. *SIAM J. Sci. Comput.*, 18:1553-1570, 1997

[32] P.K. Sweby. High resolution schemes using flux limiters for hyperbolic conservation laws. *SIAM journal on numerical analysis*. 21:995-1011, 1984

[33] A. Harten. High resolution schemes for hyperbolic conservation laws. *J. Comput. Phys.*, 49:357-393, 1983

[34] B. van Leer. Towards the ultimate conservative difference scheme. II. Monotonicity and conservation combined in a second-order scheme. *J. Comput. Phys.*, 14:361-370, 1974

[35] C.K.W. Tam, *Computational aeroacoustics: a wave number approach*. Vol. 33. 2012: Cambridge University Press.

[36] M. Popescu, W. Shyy, and M. Garbey. Finite volume treatment of dispersion-relation-preserving and optimized prefactored compact schemes for wave propagation. *Journal of Computational Physics*. 210:705-729, 2005

[37] J. Berland, C. Bogey, and C. Bailly. Low-dissipation and low-dispersion fourth-order Runge–Kutta algorithm. *Computers & Fluids*. 35:1459-1463, 2006

[38] B. Einfeldt. On Godunov-type methods for gas dynamics. *SIAM Journal on Numerical Analysis*. 25:294-318, 1988

[39] P.L. Roe. Approximate Riemann solvers, parameter vectors, and difference schemes. *J. Comput. Phys.*, 43:357-372, 1981

[40] T.W. Roberts. The behavior of flux difference splitting schemes near slowly moving shock waves. *J. Comput. Phys.*, 90:141-160, 1990

[41] Y. Stiriba and R. Donat. A numerical study of postshock oscillations in slowly moving shock waves. *Computers & Mathematics with Applications*. 46:719-739, 2003

[42] J. Delfs, An overlapped grid technique for high resolution CAA schemes for complex geometries, *7th AIAA/CEAS Aeroacoustics Conference and Exhibit*. 2001, American Institute of Aeronautics and Astronautics.

[43] R. Guenanff, P. Sagaut, E. Manoha, M. Terracol, and R. Lewandowsky, Theoretical aspects of a multidomain high-order method for CAA, *9th AIAA/CEAS Aeroacoustics Conference and Exhibit*. 2003, American Institute of Aeronautics and Astronautics.

[44] G. Cunha and S. Redonnet. On the signal degradation induced by the interpolation and the sampling rate reduction in aeroacoustics hybrid methods. *International Journal for Numerical Methods in Fluids*. 71:910-929, 2013

[45] C. Bogey and C. Bailly. A family of low dispersive and low dissipative explicit schemes for flow and noise computations. *Journal of Computational Physics*. 194:194-214, 2004

CRediT Author Statement

U S Vevek: Methodology, Software, Validation, Formal analysis, Investigation, Data curation, Writing – Original draft, Writing – Review & editing, Visualization

Basman Elhadidi: Conceptualization, Methodology, Validation, Formal analysis, Writing – Review & editing, Supervision, Project administration, Funding acquisition

Wai Lee Chan: Conceptualization, Methodology, Validation, Formal analysis, Resources, Writing – Review & editing, Supervision, Project administration, Funding acquisition